Journal of Photochemistry & Photobiology, A: Chemistry 444 (2023) 114956

Contents lists available at ScienceDirect

Journal of Photochemistry & Photobiology, A: Chemistry

journal homepage: www.elsevier.com/locate/jphotochem

Boosting the photoexcited charge collection and transportation via $BiVO_4$/Fe-TiO_2 NRs in Type-II heterojunction for efficient photoelectrochemical water splitting

Fazeelat Rehman [a], Noor Alam [a], Manzar Sohail [a], Muhammad Ahmad [c], Muhammad Israr Siddiqui [b], Muhammad Imran Irshad [d], Asad Mumtaz [a,*]

[a] Department of Chemistry, School of Natural Sciences (SNS), National University of Sciences & Technology (NUST), H-12, Islamabad 44000, Pakistan
[b] Institute of Civil Engineering, National University of Sciences & Technology (NUST), H-12, Islamabad 44000, Pakistan
[c] Department of Chemistry, Division of Science and Technology, University of Education, Lahore 44770, Pakistan
[d] Department of Physics, Khawaja Fareed University of Engineering and Information Technology (KFUEIT), Rahim Yar Khan 64200, Pakistan

ARTICLE INFO

Keywords:
Hydrothermal
1 Dimensional
Doped Titania Nanorods
Type-II Heterojunction
Photoelectrochemical
Water Splitting

ABSTRACT

Photoexcited charge separation and their efficient transportation in bulk as well as in heterojunction based photocatalysts is a challenging issue. Therefore, seeding free $BiVO_4$@Fe-TiO_2 NRs heterojunction is developed to have molecular extrinsic defects via Fe doping in TiO_2 nanorods (NRs) as a strategy in type-II heterojunctions for photoelectrochemical water splitting. Structural characterizations of $BiVO_4$@Fe-TiO_2 NRs confirm the introduction of extrinsic defects in doped Fe-TiO_2 NRs. Morphological studies evaluate the homogeneous deposition of $BiVO_4$@Fe-TiO_2 NRs to form core–shell heterostructure. In photoelectrochemical studies, $BiVO_4$@0.2 %Fe-TiO_2 shows highest photocurrent density of 1.52 mA/cm^2 in comparison to $BiVO_4$@undoped TiO_2 NRs with 0.52 mA/cm^2 and pristine TiO_2 NRs with 45μA/cm^2 at 1.23 vs. RHE under 100 mW/cm^2 light intensity. These findings elucidate the importance of modified host substrates of Fe-TiO_2 NRs to extract photoexcited electrons from guest $BiVO_4$ that has enhanced PEC performance with maximum electron mobility, efficient interfacial charge transfer and enhanced electron quenching window in type-II heterojunctions.

1. Introduction

Hydrogen energy production by sustainable renewable resources is an efficient alternative to meet the needs of the energy crisis [1]. For the purpose, water splitting via photocatalysts involves three steps; the generation of electron/hole pair charge carriers by photons, their separation and finally the surface oxidation/reduction reaction through transfer or extraction of electron/hole pair charge carriers [2]. Among the metal oxides, TiO_2 is pre-owned material for applications like DSSC, sensors, photovoltaic devices and hydrogen generation via water splitting using renewable energy resources of water and solar light [3]. TiO_2 attracted the researchers because of its low cost, high stability and non-toxicity [4]. Contrarily, it also has issues of low surface area, poor charge penetration depths and its large band gap of 3.03 eV that absorbs UV light contributing only 3 to 5 % of solar spectrum [5]. Additionally, TiO_2 has higher average effective masses, consequently migration of charges from bulk to surface is boosted which can cause surface recombination [6]. To overcome issues of TiO_2, many researchers attempted its morphological modifications like nanoparticles [7,8], nano-flowers [9], nanorods [10,11] and nanotubes [12,13], doping [14], surface defects, band gap alignments while establishing hetero-junctions [15,16] *via* depositing sensitizers over host nanomaterials [17–21].

Moreover, Hydrothermal synthesis methods for preparation of substrate TiO_2 NRs or nanotubes are utilized [22] but little attention has been given on better interfacial interactions that has been reported in several reports followed by low temperature synthesis method as sol–gel, spin coating, sputtering, dip coating, doctor blade method, chemical bath deposition methods (CBD) [20,21] for the sensitizer loading on substrate in bilayer system. Although low temperature synthesis methods are cost effective but may cause interfacial impurities at the heterojunction interfaces leading to high charge transfer resistance, higher recombination rates and poor band bending alignments

Abbreviations: PEC, Photoelectrochemical; CBD, Chemical Bath Deposition; NRs, Nanorods; 1D, one Dimensional.

* Corresponding author.
E-mail address: asad.mumtaz@sns.nust.edu.pk (A. Mumtaz).

https://doi.org/10.1016/j.jphotochem.2023.114956
Received 18 April 2023; Received in revised form 19 May 2023; Accepted 14 June 2023
Available online 19 June 2023

[19,20,23].

The development of heterojunctions while aligning band gaps proved to be an efficient approach for light harvesting with broader solar spectrum, better charge separation and fast transportation during testing of PEC water splitting [23,24]. Among different metal oxide photocatalysts, $BiVO_4$ is a potential candidate for higher solar light harvesting but it has severe long term stability issues [25,26]. Therefore, it is required to develop the heterojunction of $BiVO_4$ with other semiconductors such as metal oxides, metal sulfides and metal nitrides to avoid its photo corrosion. G. Fang et al. develop heterojunction of $BiVO_4$ with NiFeOOH and CoPi as a co-catalyst to obtain its photostability [27]. $CoNi_2O$ being used as a cocatalyst to enhance the photoactivity of the $BiVO_4$[26]. B. Dong et al. introduced multi-effect point defects to improve the photoelectrochemical water splitting of $BiVO_4/TiO_2$ photoanode heterojunctions [28]. Rh_2O_3 cocatalyst was used to enhance the water splitting of $BiVO_4$ via fast charge transportation and improving surface kinetics [29]. S. Zhang et al. developed Oxygen defects to hance the photoactivity of ZnFe-LDH [30]. Magnetic and thermal external field effects were applied to $NaNbO_3$ to enhance its photoelectrochemical water splitting performance [31]. L. Gao et al. developed $AgVO_3$ heterojunction with Mo doped $BiVO_4$ for efficient charge separation and fast transportation [32].

In this work, photoexcited charge separation and transportation properties of $BiVO_4$ @Fe-TiO_2 NRs type-II heterojunctions were investigated as a function of sensitizer loading and temperature, over undoped and doped Fe-TiO_2 NRs. $BiVO_4$ is used as representative sensitizer as potential candidate of photoexcited charge carries, and undoped/doped Fe-TiO_2 NRs are used as potential substrates to extract the photoexcited charge carriers of the sensitizer. Morphological studies showed the homogeneous deposition of 0.2 M $BiVO_4$ at 0.2% Fe doped and undoped TiO_2 NRs with controlled core–shell structure for efficient interface stability and photochemical activity. Hydrothermally synthesized $BiVO_4$@0.2% Fe doped TiO_2 NRs demonstrated maximum photoconversion, photostability and charge transportation across the circuit due to optimized substrate engineering and sensitizer loading. Electrochemical impedance spectroscopy showed the enhanced extraction of photoexcited charges by 0.2% Fe doped TiO_2 NRs from $BiVO_4$ which is due to resultant core–shell morphology, interface stability, establishment of efficient heterojunction via quasi-Fermi level adjustment between constituted $BiVO_4$ and Fe-TiO_2 NRs heterojunctions. These outcomes demonstrated the importance of substrate and interfacial engineering to improve the efficiencies of type-II heterojunctions.

2. Experimental section

Materials. All chemicals were used without any purification and were of analytical grade. Titanium *n*-butoxide was obtained from Sigma Aldrich. Pure salts of bismuth nitrate hexahydrate, vanadium pentoxide and iron chloride ($FeCl_3$) were also purchased from Sigma Aldrich and used as received without any further purification. Hydrochloric acid (37% HCl), acetonitrile and nitric acid (HNO_3) of analytical grade were purchased from Fluka.

1) The fabrication of TiO_2 Nanorods on FTO. TiO_2 Nanorods were directly synthesized on Fluorine doped tin oxide (FTO) substrate *via* hydrothermal process. FTO was cleaned by sonication with ethanol, acetone and deionized water for 15 min in each, followed by drying in air at room temperature and cleaned FTO was confirmed by transparency in light and its standard conductivity (10–15 Ω resistance). 15 mL of each deionized water (DI) and hydrochloric acid (37% pure) was mixed to have a solution. 0.6 mL of titanium n-butoxide (97% Aldrich) was added in the above solution followed by 30 min stirring to have a parent solution. After that parent solution was poured in clean Teflon lined autoclave with 50 mL capacity. The cleaned FTO was placed with conductive side downwards in Teflon lined hydrothermal autoclave. Hydrothermal autoclave was heated up to 150 °C for 12 h. After the completion of reaction, the autoclave was cooled in air and samples were collected and rinsed with DI water followed by drying in air. Finally, TiO_2 Nanorods/FTO were annealed at 450 °C for 120 min to have crystallinity in it. For Fe doped TiO_2 Nanorods, 1 mL acetonitrile and $FeCl_3$ with three different concentrations of 2.5 mM, 5 mM and 10 mM were additionally added in the parent solution and the whole above procedure was deployed and later samples were designated as 0.1%, 0.2% and 0.3% Fe doped TiO_2 Nanorods, respectively.

2) Hydrothermal Synthesis of $BiVO_4$ Over TiO_2 and Fe-TiO_2 NRs. Both precursor solutions of bismuth nitrate (each 0.05 M) and vanadium pent oxide (each 0.05 M) were prepared in DI water and HNO_3, while continuously stirring on hot plate at 50℃. Then both these clear transparent solutions were mixed with 1:1 (each 0.05 M) with 0.1 M total concentration with volume of 20 mL. After mixing the solutions, 1 mL of acetonitrile as a ligand was added into the solution and then the solution was transferred into Teflon lined autoclave and substrate with TiO_2 Nanorods layer was placed (facing upward) into hydrothermal autoclave. This solution in hydrothermal autoclave was heated at 150 °C for 12 h to get 0.1 M $BiVO_4$. After the reaction period the autoclave was cooled, and sample with loading of 0.1 M $BiVO_4$ @TiO_2 Nanorods was separated and rinsed with water. Following this procedure to check the effect of concentration of precursor (0.2 M, 0.3 M and 0.4 M) as 0.2 M $BiVO_4$@TiO_2, 0.3 M $BiVO_4$@TiO_2 and 0.4 M $BiVO_4$@TiO_2 with 1 mL of acetonitrile were prepared. After drying in air, all the samples were annealed in chamber furnace at 450 °C for 120 min. Moreover, synthesis of $BiVO_4$ with 0.2 M concentration was optimized over TiO_2 and 0.1%, 0.2% and 0.3% Fe doped TiO_2 NRs to have core–shell (0.2 M $BiVO_4$@Fe-TiO_2) structures. Furthermore, the effect of temperature (150, 175, and 200 °C) during hydrothermal synthesis of 0.2 M $BiVO_4$ over 0.2% Fe doped TiO_2 Nanorods was investigated with samples designated as 0.2 M $BiVO_4$@0.2% Fe-TiO_2 NRs at 150 °C, 175-0.2 M $BiVO_4$@0.2% Fe-TiO_2 NRs at 175 °C and 0.2 M $BiVO_4$@0.2% Fe-TiO_2 NRs at 200 °C. Schematic diagram of the photoanodes are presented in Scheme 1.

3. Material characterizations

Crystalline structure and phase identification of $BiVO_4$/Fe-TiO_2 NRs were done by using X-ray diffraction (XRD; Bourevestnik dron 8 PXRD) with an excitation wavelength of ($\lambda = 1.5405$ A°) in the range of 10-80°. To observe the nanostructured morphology and to obtain the elemental analysis of the sample, Scanning Electron Microscopy (SEM, JSM-6490) and Energy-Dispersive X-ray Spectroscopy (EDS, VEGA3 LMU) were used. For TEM Characterizations, Zeiss module is used with high resolution. UV–Vis Diffuse Reflectance spectra were measured after the standard baseline correction with PerkinElmer UV/Vis Lambda 365, between the wavelength of 300–800 nm. The Raman scattering analysis was performed (Renishaw 2000 spectrometer) with the incident wavelength of 632 nm to determine Raman vibrational modes of the photocatalyst. Fourier transform infrared spectroscopy (FTIR; Bruker FTIR alpha) was used to determine various functional groups and their stretching or bending vibrations in a functional group or fingerprint region in the range of 4000–500 cm^{-1}. Photoluminescence spectroscopy (PL; PerkinElmer Fluorescence Spectrometer, FL-6500) was performed to determine the excitation-emission spectra at 400 nm excitation wavelength.

3.1. Photoelectrochemical studies

To determine the photoelectrochemical activity of all the prepared photocatalysts, electrochemical workstation equipped with Potentiostat/Galvanostat/ZRA (Model; INTERFACE1000E-12095) in a three-electrode setup is used with $BiVO_4$/Fe-TiO_2 Nanorods as a working electrode with 1 cm^2 active exposed surface area, a Pt wire was taken as a counter electrode and Ag/AgCl ($E_{Ag/AgCl} = 0.197$) with saturated (3 M) KCl was used as a reference electrode under light illumination. Solar light simulator was used as the light source and its intensity was calibrated with a standard silicon solar cell and controlled at 100 mW/cm^2

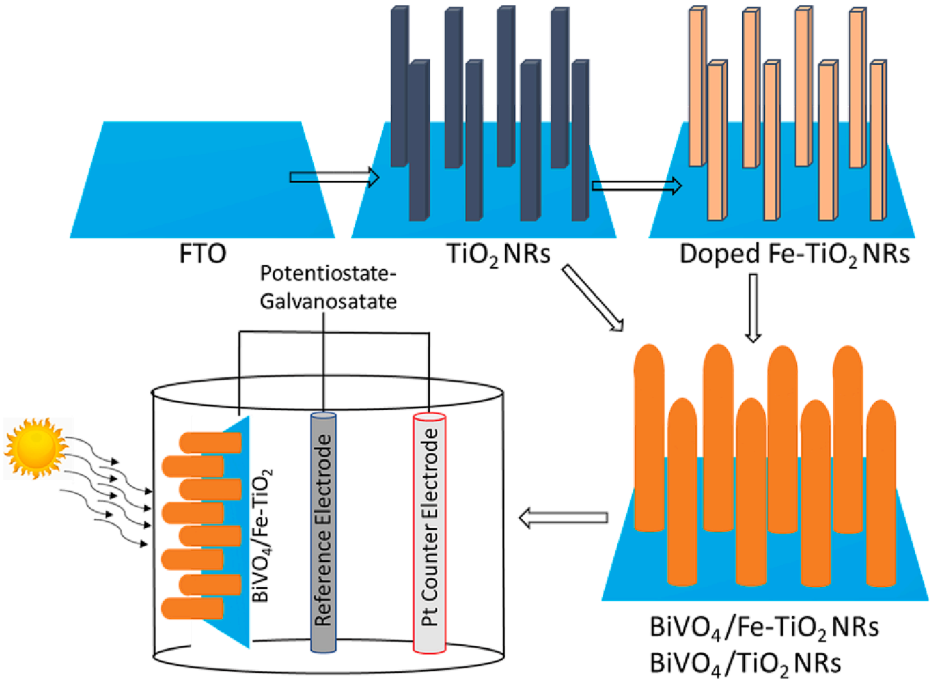

Scheme 1. Schematic diagram of the development of $BiVO_4$@Fe-TiO_2 NRs and PEC water splitting.

(AM 1.5 illumination). To remove the dissolved oxygen, Ar gas was bubbled through aqueous electrolyte prior to the measurements. PEC measurements were performed using Ag/AgCl reference electrode in the presence of 0.5 M Na_2SO_4 buffered to the pH 7. Linear sweep voltammetry was recorded against Ag/AgCl of the working electrode at a scan rate of 20 mV/s. The voltage was optimized between −0.5 V to 1 V vs. Ag/AgCl. The measured potential was converted into reversible hydrogen potential (RHE) vs. Ag/AgCl using the following equation.

$$E_{RHE} = E_{Ag/AgCl} + 0.059.pH + E^{\circ}_{Ag/AgCl} \quad (1)$$

4) Here E_{RHE} shows the converted potential vs. RHE, $E_{Ag/AgCl}$ represent the experimental potential measured against the Ag/AgCl reference electrode, $E^{\circ}_{Ag/AgCl}$ is the standard potential of Ag/AgCl (0.197). Chronoamperometry (I-t) technique was performed to study the stability of the photocatalysts at a potential of 0.3 V against Ag/AgCl reference (1.23 V vs. RHE) electrode under light illumination. Electrode-electrolyte interface and electrochemical impedance spectroscopy were performed on the same workstation under the open–circuit condition (OCP) in dark and light with the frequency range from 0.2 Hz to 100 kHz at an AC potential amplitude of 10 mV under open circuit potential (OCP). Flat band potential study was done by Mott-Schottky measurements at 1 kHz frequency under a dark environment in the voltage window of −0.5 V to + 0 V vs Ag/AgCl electrode. A schematic diagram of the PEC water splitting with three electrode assembly is presented in scheme 1.

4. Results and discussion

4.1. Morphological and Structural Studies:

Structural properties of the synthesized photocatalytic materials are investigated using X-ray diffraction pattern as shown in Fig. 1. In Fig. 1a, pristine TiO_2 on FTO showed tetragonal crystal system with rutile phase and it also showed the hydrothermally dominant growth along [002] plane [33]. The characteristic peaks at 2θ value of 27.28°, 36.13°, 41.73°, 54.8° and 63.35° for rutile phase of TiO_2 nanorods attributed to (110), (101), (111), (211) and (002) planes, respectively [34]. Also, (101) plane is a dominating plane in pristine rutile TiO_2 lattice with maximum stability and least energy, while upon doping with iron, (002) is originating as a dominant plane in 0.1% and 0.2% Fe doped TiO_2 NRs. On the other hand, 0.3% doping of Fe in rutile TiO_2 NRs decelerates the growth in the direction of [002] facet. While, peaks at 2θ value of 27.13°, 34.3°, 38.6°, 51.9°, 62°, 65.9° and 70.4° belongs to the FTO [34]. Similarly, for $BiVO_4$ peaks observed at 2θ values of 18.8°, 29.1°, 30.75°, 34.2, 35.4°, 40.2°, 42.77°, 46.1°, 47.05°, 47.5°, 50.57°, 53.6°, 58.37°, and 59.65° correspond to (011), (121), (040), (200), (002), (211), (015), (132), (240), (042), (202), (161), (321) and (123) planes, respectively (JCPDS NO 01–078-1534 and 14-0688). To see the effect of loading of $BiVO_4$ over TiO_2 NRs at 150 °C, different concentration of 0.1 M, 0.2 M, 0.3 M and 0.4 M of $BiVO_4$ are used as shown in Fig. 1a. It is observed that as the loading of $BiVO_4$ over TiO_2 NRs increases, the intensity of corresponding peaks also increased and there are no extra peaks observed as impurity peaks other than the designated $BiVO_4$@TiO_2 NRs which confirmed the composite formation without changing specific crystal phase [35].

Furthermore, XRD patterns of Fe doped TiO_2 NRs are investigated as shown in Fig. 1b. XRD pattern in doped and un-doped TiO_2 NRs showed slight shift towards lower 2θ value upon Fe doping with 0.1%, 0.2% and 0.3% of Fe-TiO_2 [36,37], illustrate the successful doping of Fe into the TiO_2 crystal structure [38] as depicted into Fig. 1b. Briefly, the peak of TiO_2 at 70.4° shifted to 70° for 0.1% Fe doped TiO_2, to 69.8° for 0.2% Fe doped TiO_2 and to 69.4° for 0.3% Fe-TiO_2 doped NRs. Similarly peak at 2θ value of 62° shifted to 61.9° for 0.1% Fe-TiO_2, to 61.8° for 0.2% Fe-TiO_2 and to 61.6° for 0.3% Fe-TiO_2 NRs as depicted in Fig. 1b [39]. Hence, by increase in doping content peak shifting increases which confirmed the increase in doping content of Fe into TiO_2 NRs (Fig. 1b). As depicted in the Fig. 1c, XRD pattern for temperature profile showed a decrease in intensity of peaks at 2θ values of 18.8°, 29.1° and 40.2° which are indexed to (011), (121) and (211) planes, respectively, for 0.2 M $BiVO_4$ with increase in temperature from 150 °C to 175 °C and 200 °C, indicating a decrease in particle sizes of $BiVO_4$ is observed [40].

The surface morphologies of pristine TiO_2 and modified $BiVO_4$@Fe doped TiO_2 NRs are illustrated in Fig. 2 using SEM images. In Fig. 2a, the top view of TiO_2 Nanorods is shown covering the whole surface of FTO substrate. TiO_2 NRs having rough tips are supporting the perpendicular growth pattern along [002] plane in support to XRD results with square

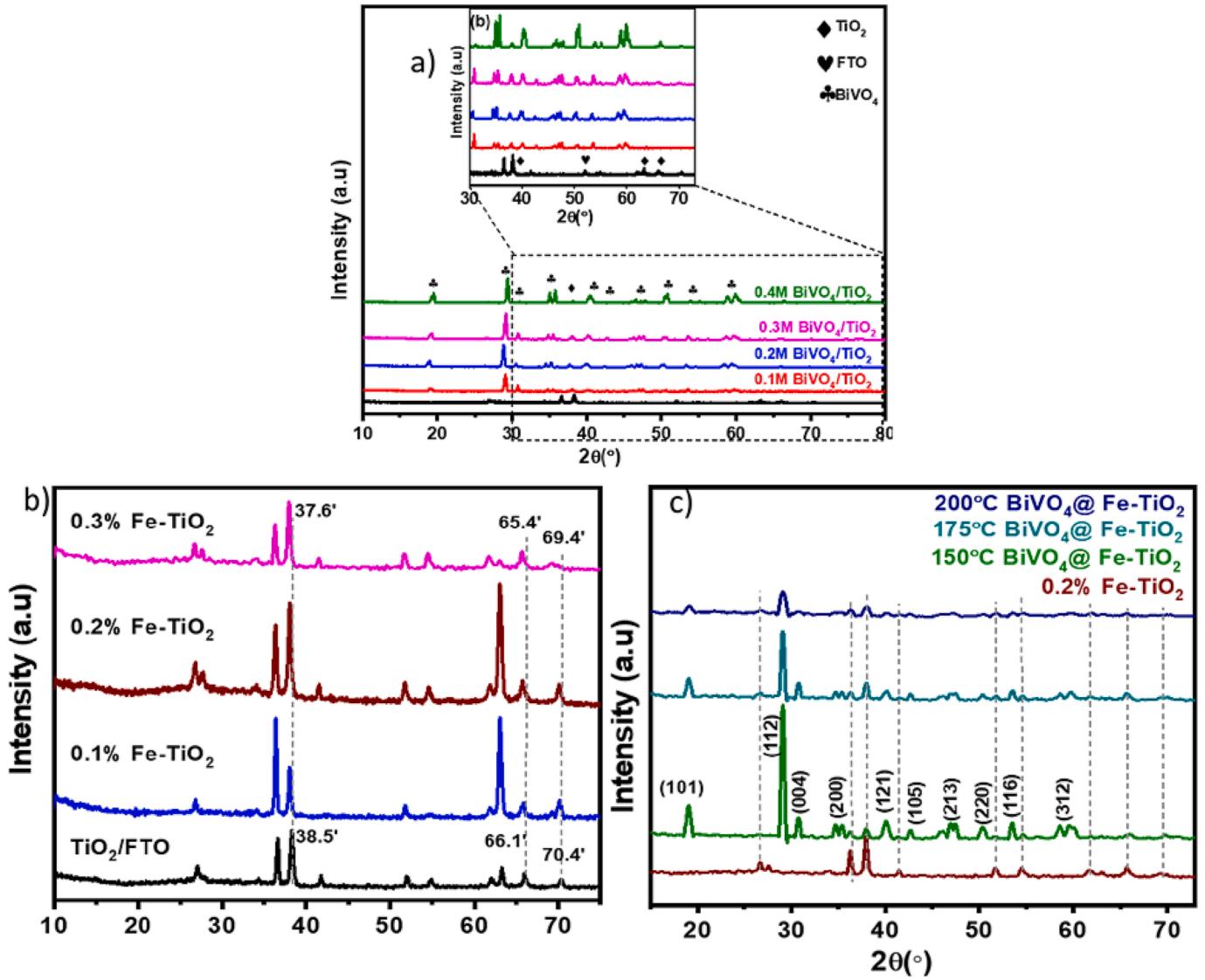

Fig. 1. XRD pattern of (a) pristine TiO_2 NRs and 0.1 M, 0.2 M, 0.3 M, 0.4 M precursor concentration for deposition of $BiVO_4$ over TiO_2 NRs at 150 °C, (b) 0.1%, 0.2% and 0.3% Fe doped TiO_2 NRs, c) 0.2 M $BiVO_4$ deposited at three different temperatures of 150 °C, 175 °C, 200 °C over 0.2% Fe doped TiO_2 NRs.

shaped diameter are signifying the tetragonal crystal system as expected from growth mechanism. In Fig. 2b and 2c, it is observed that uniform deposition of $BiVO_4$ on TiO_2 NRs illustrating the core–shell TiO_2@$BiVO_4$ morphology. In Fig. 2b-e, it is observed that with increase in concentration of precursors from 0.1 M to 0.2 M, 0.3 M, and 0.4 M, $BiVO_4$ loading is increasing. 0.1 M and 0.2 M $BiVO_4$ deposition concentration shows the uniform loading of $BiVO_4$ sensitizer onto TiO_2 NRs as presented in Fig. 2b and 2c with optimized core–shell TiO_2-$BiVO_4$ nanostructure, while in Fig. 2d and 2e the loading is higher which covers the TiO_2 NRs surface with nanorods and nano bullets of $BiVO_4$ by 0.3 and 0.4 M of precursors, respectively, illustrating 0.2 M optimized precursor for $BiVO_4$ loading over TiO_2 NRs, keeping the core–shell morphology for enhanced interfacial interaction of sensitizer@host ($BiVO_4$@TiO_2 NRs) heterojunction. Moreover, 0.2 M precursor concentration is used to deposit $BiVO_4$ over 0.2% Fe-TiO_2 NRs at increased temperatures of 175 °C and 200 °C. It is observed that core–shell morphology is maintained even at 175 °C with homogeneous and thick deposition layer of $BiVO_4$ over 0.2% Fe-TiO_2 NRs as shown in Fig. 3a (low to high resolution SEM images). While morphology of $BiVO_4$ changes to horizontal random nanofibers over Fe-TiO_2 NRs at 200 °C over 0.2% Fe-TiO_2 NRs as shown in Fig. 3b. Importantly, 0.2 M precursor concentration for synthesis of $BiVO_4$ over 0.2 %Fe-TiO_2 NRs shows the homogeneous morphology with good control over the synthesis method. EDX analysis shows the elemental composition of $BiVO_4$@0.1 %Fe-TiO_2 NRs, $BiVO_4$@0.2 %Fe-TiO_2 NRs and $BiVO_4$@0.3 %Fe-TiO_2 NRs (Fig. S1). The EDX spectra in Fig. S1 shows the decrease in appeared concentration of Ti by increasing the concentration of Fe doping in TiO_2 NRs, while maintaining $BiVO_4$ as sensitizer. EDX in Fig. S1 confirms the presence of respective elemental percentages and content of Fe dopant which replaced the Ti is 0.1% for 2.5 mM, 0.22 atom % for 5 mM and 0.3% for 10 mM doping concentration. To check the homogeneity and uniformity of elements in heterojunctions, 0.2 M $BiVO_4$@TiO_2 NRs synthesized at 150 °C and 0.2 M $BiVO_4$@0.2 %Fe-TiO_2 NRs synthesized at 175 °C are further analyzed using mapping analysis. Elemental mapping confirmed the homogeneous and uniform distribution of elements present in $BiVO_4$@TiO_2 NRs (Fig. S2a) and $BiVO_4$@0.2 %Fe-TiO_2 NRs (Fig. S2b) heterojunction on FTO substrate. This homogeneity may help the overall charge transfer of photoexcited electrons across the interfaces in heterojunctions.

Topography study shows the increase in surface roughness by increasing loading of $BiVO_4$ over Fe modified TiO_2 NRs using optical profilometer (micro scale) that is in good agreement with the XRD and SEM results. The surface roughness increases as 0.0326%, 0.0363%, 0.0906% and 0.140% for TiO_2, 0.2% Fe-TiO_2, 150 °C 0.2 M $BiVO_4$@-TiO_2, and 175 °C 0.2 M $BiVO_4$@Fe-TiO_2 NRs, respectively, as shown in

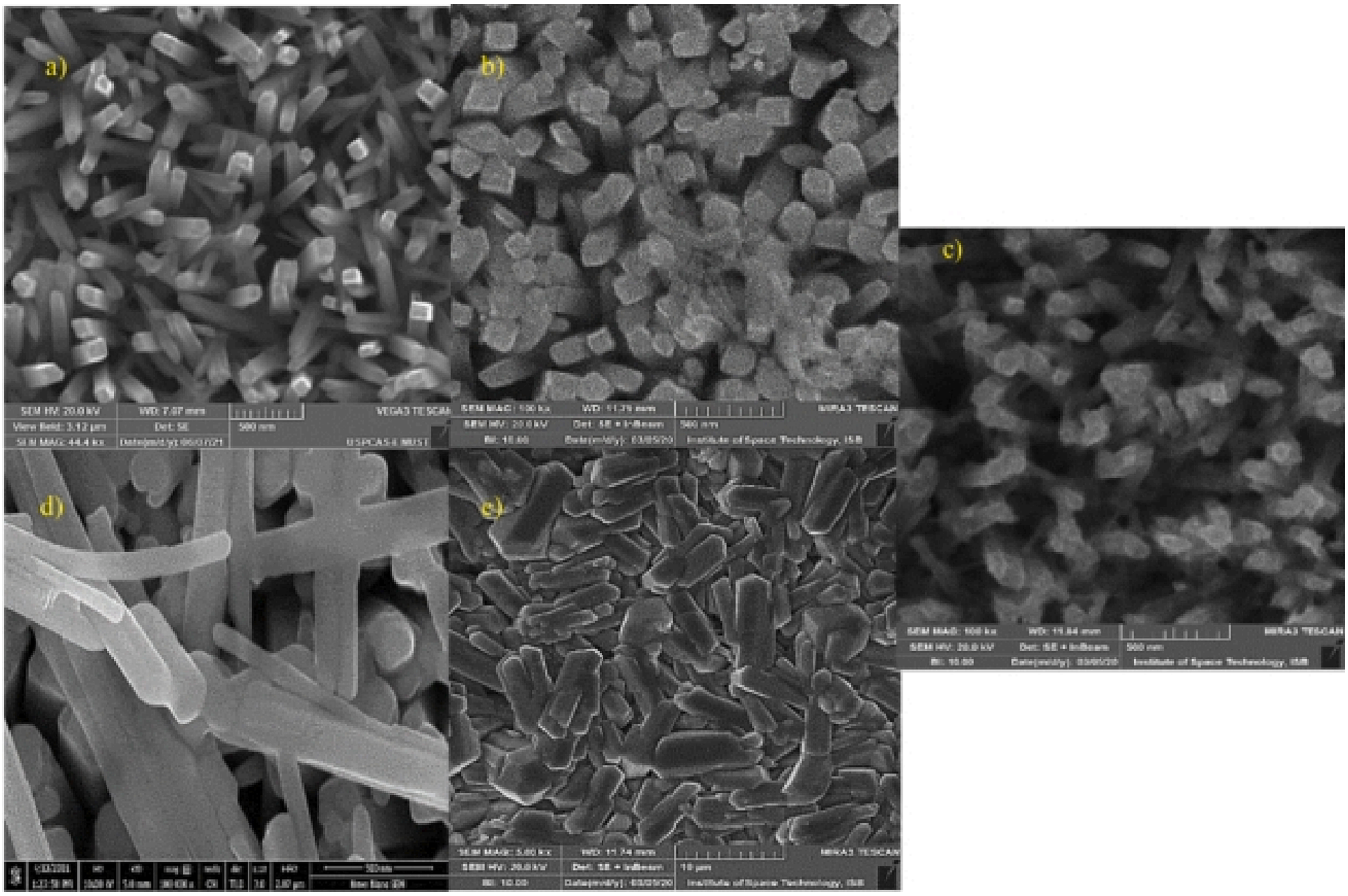

Fig. 2. SEM images of a) Pristine TiO_2 NRs and precursor concentrations for $BiVO_4$ deposition over TiO_2 NRs using; b) 0.1 M, c) 0.2 M, d) 0.3 M, and e) 0.4 M.

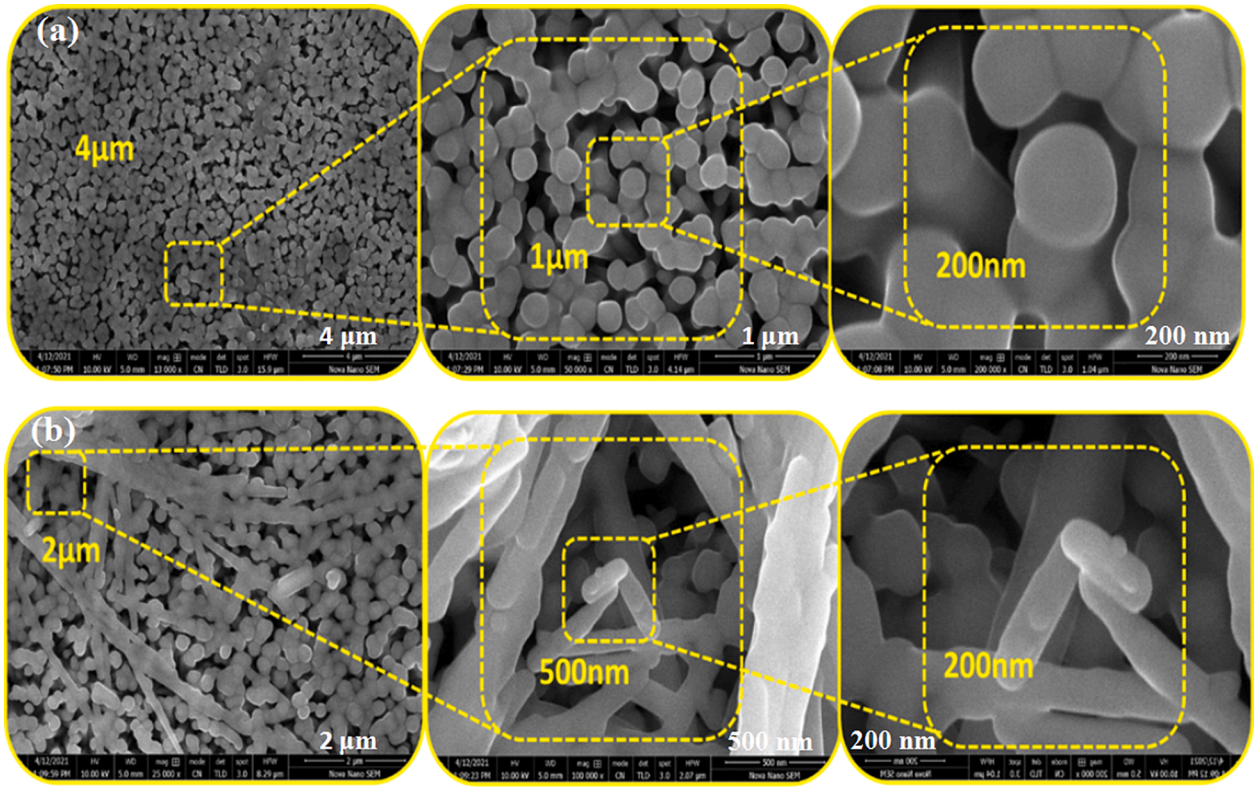

Fig. 3. SEM images of 0.2 M $BiVO_4$ deposition upon 0.2% Fe-TiO_2 NRs at (a) 175° C and (b) 200 °C.

Table S1. The increased surface roughness is always linked with extra scattering loss, suggesting the lower transmittance, and consequently increase in absorbance of the heterojunction photocatalysts.

Transmission Electron microscopy is used to determine the morphology and homogeneity of the deposition of $BiVO_4$/0.2 %Fe-TiO_2 NRs as shown in Fig. 4. Fig. 4a and 4b are evidencing the nanorod like morphology of $BiVO_4$/Fe-TiO_2 NRs. The average diameter of 0.2% Fe-TiO_2 NRs is calculated to be 133 nm and the diameter of $BiVO_4$/Fe-TiO_2 NRs is found to be 177 nm. Also, homogeneous deposition of $BiVO_4$ is observed along the walls of the 0.2% Fe-TiO_2 NRs (Fig. 4b). Fig. 4c and 4d shows the development of heterojunction between $BiVO_4$ and 0.2% Fe-TiO_2 NRs. The deposition of the $BiVO_4$ over Fe-TiO_2 NRs is homogeneous and a core–shell Fe-TiO_2 NRs -$BiVO_4$ is evident from this study. These results are in good agreement with the SEM results indicating the core–shell morphology of $BiVO_4$/Fe-TiO_2 NRs. Moreover, the d-spacing is found to be 0.30 nm indicating the presence of 121 phase of the $BiVO_4$ in Fig. 4e. Furthermore, in Fig. 4f, the inverse fast Fourier Transform (IFFT) was applied to Fig. 4e, and it is observed that $BiVO_4$ with 121 phase shows the dominant phase among the others. These results are in good agreement with the XRD results.

4.2. Optical and structural studies

For optical properties, % diffuse reflectance of Fe modified TiO_2 NRs, unmodified pristine TiO_2 NRs, $BiVO_4$, $BiVO_4$@TiO_2 and $BiVO_4$@Fe-TiO_2 NRs were measured in the range of 350 to 900 nm as shown in Fig. 5. In % reflectance spectra of Fig. 5a, the pristine TiO_2 NRs showed the maximum reflectance of 35–40% in the visible region, hence, minimum absorbance in visible region as compared to other $BiVO_4$, and $BiVO_4$@TiO_2 NR arrays. On the other hand, pure $BiVO_4$/FTO shows % reflectance of nearly 25% in visible region of 500–700 nm range (Fig. 5a). Loading of $BiVO_4$ on TiO_2 NRs increases, by increasing stoichiometric concentration of each Bi and V precursors, such as 0.1 M, 0.2 M, 0.3 M and 0.4 M, which can be clearly observed from their decrease in % reflectance of 29%, 30%, 26% and 20%, respectively, indicating higher photon capturing efficiency and is in good agreement with XRD and SEM results (Fig. 5a). Similarly, the % reflectance of TiO_2 NRs is observed to be 35–40% in the whole range of 350–900 nm range while % reflectance of 0.1% Fe-TiO_2, 0.2% Fe-TiO_2 and 0.3% Fe-TiO_2 NRs are observed to be 27%, 21% and 25% in the visible spectrum range of 520–700 nm, respectively, as shown in Fig. 5b, indicating the maximum absorbance of 0.2% Fe-TiO_2 NRs by increasing bulk and surface defects via Fe replacement with the Ti in TiO_2 lattice in comparison to pristine TiO_2 NRs. Moreover, 0.2 M concentration of each Bi and V precursor were used to synthesis $BiVO_4$ at 150 °C, 175 °C and 200 °C over 0.2% Fe-TiO_2 NRs and it is observed that % reflectance is further decreased to minimum 17% after loading 0.2 M $BiVO_4$ sensitizer on 0.2% Fe-TiO_2 NRs for 175 °C $BiVO_4$@0.2 %Fe-TiO_2 bilayer heterojunction in comparison to 150 °C $BiVO_4$@0.2 %Fe-TiO_2 (>21% reflectance) and 200 °C $BiVO_4$@0.2 %Fe-TiO_2 (>20% reflectance) in the visible range of 400–700 nm as shown in Fig. 5c, indicating that $BiVO_4$@0.2 %Fe-TiO_2 are now capable of harvesting maximum visible light in the range of 400–700 nm in comparison to 0.2 M $BiVO_4$@TiO_2 NRs. It shows that crystallinity of sensitizer $BiVO_4$ over 0.2% Fe-TiO_2 may play a crucial role in absorbing photons from solar light. In addition to Fig. 5, the thin film photocatalysts are observed apparently and they are also showing prominent color changes as shown in Fig. S3 (subset) along with their specific band gap tunings in heterojunctions of $BiVO_4$@TiO_2 and $BiVO_4$@0.2 %Fe-TiO_2. By increasing deposited $BiVO_4$, there is an increase in the intensity of color of the photocatalyst thin films from white to yellowish to orange by increasing deposition of sensitizer $BiVO_4$ over Fe-TiO_2 NRs. The band gap energies of photocatalysts were calculated by using the equation; $(\alpha h\vartheta)^{1/n} = B(h\vartheta - Eg)$ by plotting graphs between $(F(R)hv)^{1/2}$ and binding energy (eV), where, *F(R), h, v* are Kubelka Munk function, Planck's constant and absorption frequency, respectively, in Figs. S3a and S4b. While, $F(R) = \frac{(1-R)^2}{2R}$. The n factor is ½ or 2 for direct or indirect band gaps it depends upon nature of transition [41]. In Kubelka Munk equation α is replaced by F(R) factor and is plotted on y-axis with *hν* on x-axis to calculate band gaps as given in Table S2. Band gaps (E_g) of pristine 3.02 eV for TiO_2 NRs, 2.98 eV for 0.2% Fe-TiO_2 NRs, 2.15 eV for $BiVO_4$ edges of $BiVO_4$@TiO_2 and 2.04 eV for $BiVO_4$ edges of $BiVO_4$@0.2 %Fe-TiO_2 NRs composites are observed, indicating efficient heterojunction formation with maximum band alignment at the heterojunction of $BiVO_4$@0.2 %Fe-TiO_2 NRs at 175 °C in comparison to $BiVO_4$@TiO_2 NRs at 150 °C.

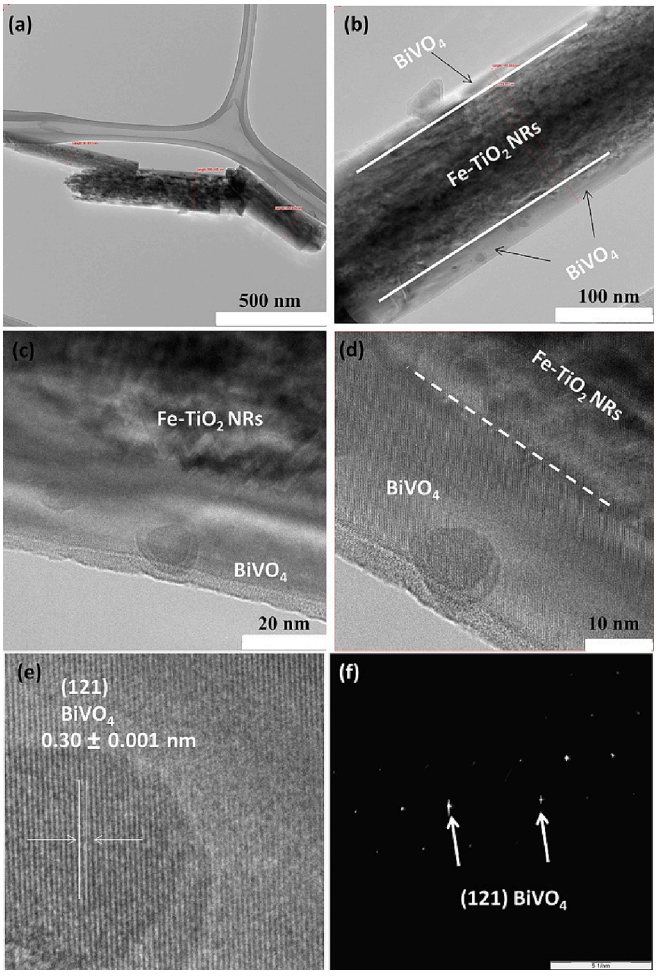

Fig. 4. TEM of $BiVO_4$/0.2% Fe-TiO_2 NRs with resolution of a) 500 nm, b) 100 nm, c) 20 nm, d) 10 nm, e and f) IFFT of thin film.

The fluorescence emission studies of synthesized photocatalysts were carried out to confirm the photoexcited charge recombination as shown in Fig. 6. Normally, the higher the intensity of the peak, higher is the recombination phenomena [19]. In Fig. 6a, TiO_2 shows the highest emission peak intensity at an excitation wavelength energy of 290 nm, in comparison to all other photocatalysts, hence, maximum recombination of charges is observed in it. While, the increase in concentration loading of $BiVO_4$@TiO_2 causes the decrease in emission intensity of fluorescence emission spectra which indicates the lower recombination of charges in Fig. 6a. In Fig. 6b, among three doped samples, 0.1% Fe-TiO_2 has maximum emission intensity after pure TiO_2 followed by 0.3% Fe-TiO_2 intensity and the minimum emission intensity is of 0.2% Fe-TiO_2, indicating the least recombination of the charges of 0.2% Fe-TiO_2 NRs. It is evident from the above results that with increasing doping content of Fe in TiO_2 NRs, extrinsic defects are introduced successfully and the defects reached to its saturation level with 0.3% Fe doping of TiO_2 NRs that triggers higher recombination rates in comparison to

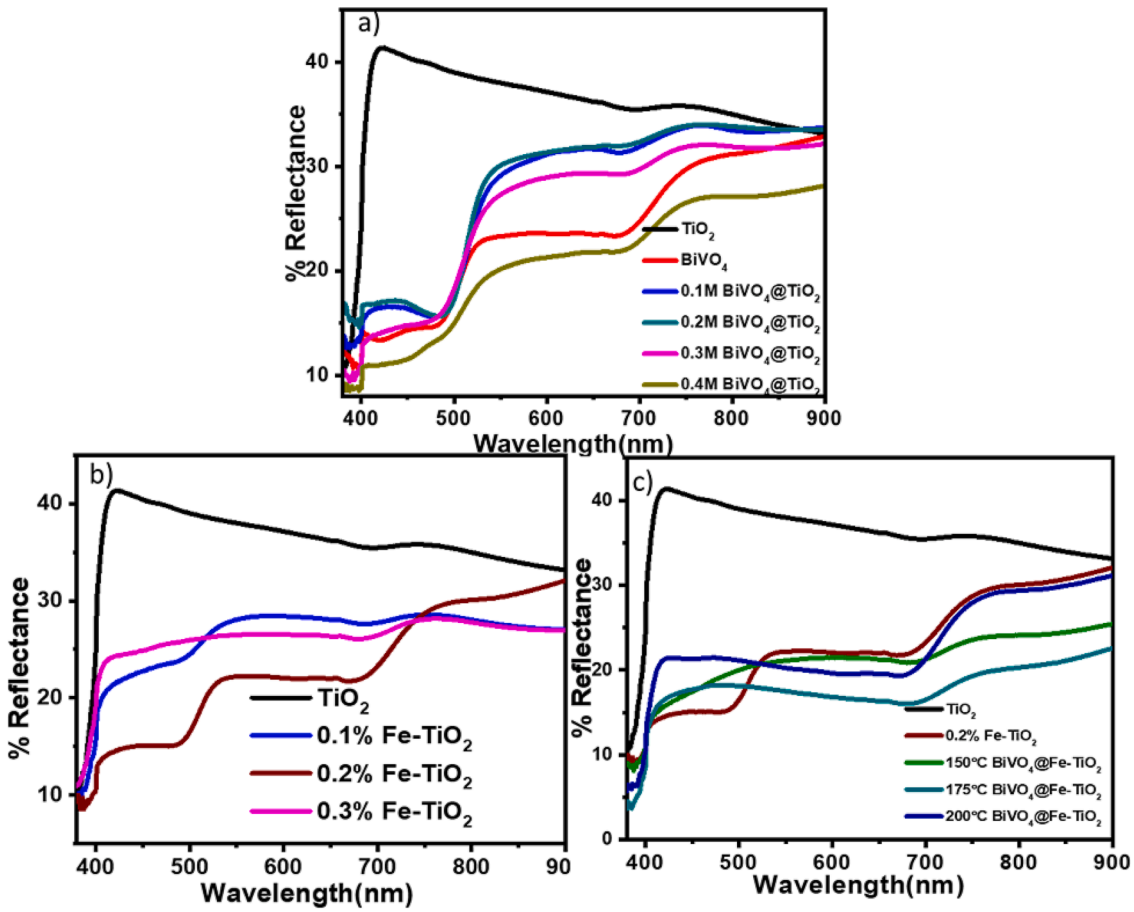

Fig. 5. UV–Visible spectrum % reflectance of a) Pristine TiO_2/FTO, Pristine $BiVO_4$/FTO and 0.1 M, 0.2 M, 0.3 M and 0.4 M precursor concentrations for $BiVO_4$ deposition upon TiO_2 NRs at 150 °C and b) 0.1% Fe-TiO_2, 0.2% Fe-TiO_2 and 0.3% Fe-TiO_2 NRs and c) 0.2 M $BiVO_4$ deposition upon 0.2% Fe-TiO_2 NRs at 150 °C, 175 °C and 200 °C.

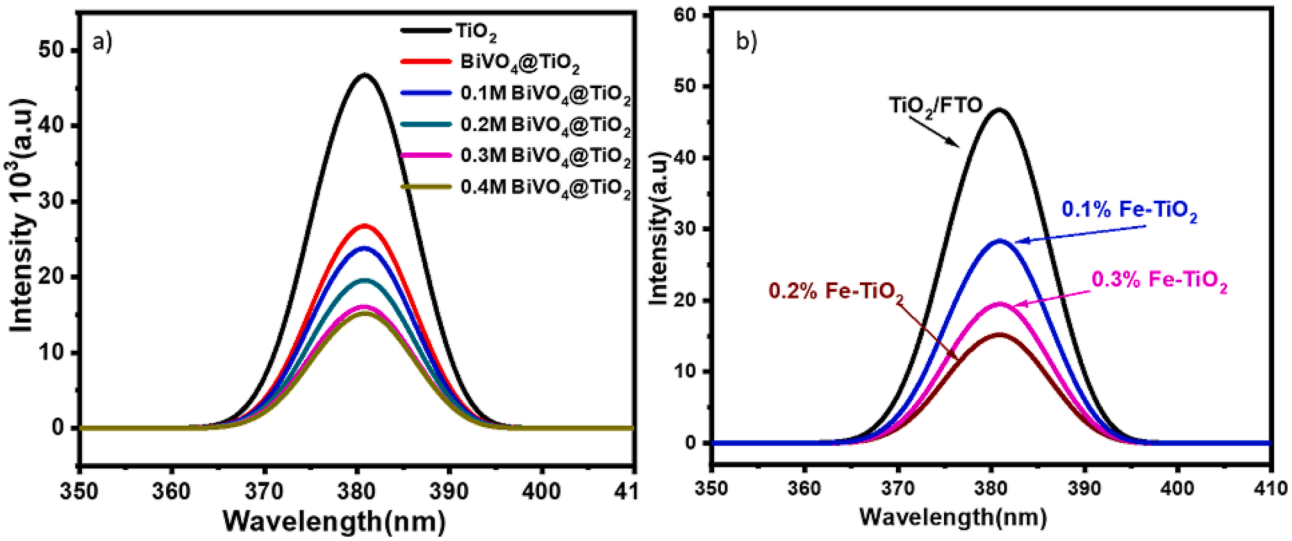

Fig. 6. Fluorescence emission spectra of a) Pristine TiO_2/FTO, Pristine $BiVO_4$/FTO and 0.1 M, 0.2 M, 0.3 M and 0.4 M precursor concentrations for $BiVO_4$ deposition upon TiO_2 NRs at 150 °C and b) 0.1% Fe-TiO_2, 0.2% Fe-TiO_2 and 0.3% Fe-TiO_2 NRs.

0.2% Fe-TiO_2 NRs [42]. This also indicates that 0.2% Fe-TiO_2 NRs can act as a better substrate for the extraction of photoexcited charges of $BiVO_4$ in $BiVO_4$@0.2% Fe-TiO_2 NRs heterojunction.

For structural evaluation of photocatalysts, the Raman spectra were studied in the range of 100–1000 cm^{-1} as shown in Fig. 7. The pristine rutile TiO_2 shows four characteristic vibrations as follows; A1g (598.2 cm^{-1}), E_g (430.7 cm^{-1}) and B1g (210.8 cm^{-1}) [43] as shown in Fig. 7a. In Fig. 7a, $BiVO_4$/TiO_2 NRs heterojunctions, exhibited an intense peak near end of the axis at 818 cm^{-1} which is attributed to symmetric stretching mode of Vs (V-O) [44]. Also, at 327 cm^{-1} and 370 cm^{-1} the

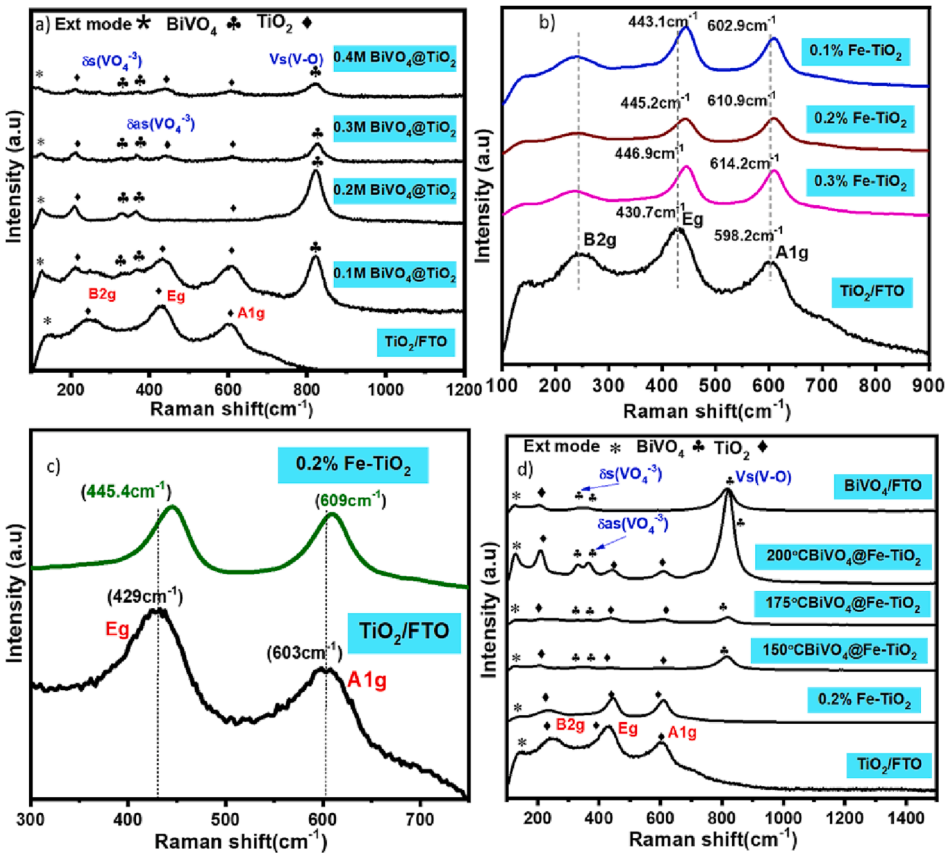

Fig. 7. Raman spectra of a) TiO_2 NRs and 0.1 M, 0.2 M, 0.3 M and 0.4 M precursor concentrations for $BiVO_4$ deposition upon TiO_2 NRs at 150 °C, b) 0.1% Fe-TiO_2, 0.2% Fe-TiO_2 and 0.3% Fe-TiO_2 NRs, c) Raman peak shifts with doping 0.2% Fe-TiO_2 and d) 0.2 M $BiVO_4$ deposition upon 0.2% Fe-TiO_2 NRs at 150 °C, 175 °C and 200 °C.

peaks assigned to symmetric and asymmetric bending of δs and δas vanadate ions, respectively. Similarly, in 0.1%, 0.2% and 0.3% doped Fe-TiO_2 at three different concentrations the shifting is observed in last two peaks of B1g, Eg and A1g bands appeared with no Fe-O vibrations, indicating the successful doping of Fe in TiO_2 NRs. In Fig. 6b, Fe doping in TiO_2 causes a slight shift in A1g peak towards right from 598.2 cm^{-1} to 602.9 cm^{-1} (for 0.1% Fe-TiO_2), 610.9 cm^{-1} (for 0.2% Fe-TiO_2) and 614.2 cm^{-1} (for 0.3% Fe-TiO_2) as shown in Fig. 7b. Similarly, E_g peak in pure TiO_2 at 430.7 cm^{-1} shifted towards right at 443.1, 445.2 and 446.9 cm^{-1} in 0.1% Fe-TiO_2, 0.2% Fe-TiO_2 and 0.3% Fe-TiO_2, respectively as shown in Fig. 7b and 6c. These results indicated that by increasing doping content of Fe in TiO_2 NRs, blue shift in peaks increases [45] and it is in good agreement with the XRD results. In Fig. 7d, upon depositing $BiVO_4$ over Fe doped TiO_2 Nanorods, the Raman peaks also showed stretching and bending of V-O same as in pure $BiVO_4$/FTO. As shown in Fig. 7d the intensity of peaks increases with temperature which indicates the increase in crystallinity of $BiVO_4$ with increase in temperature. While, maximum crystallinity is observed in 200 °C $BiVO_4$@Fe-TiO_2 NRs

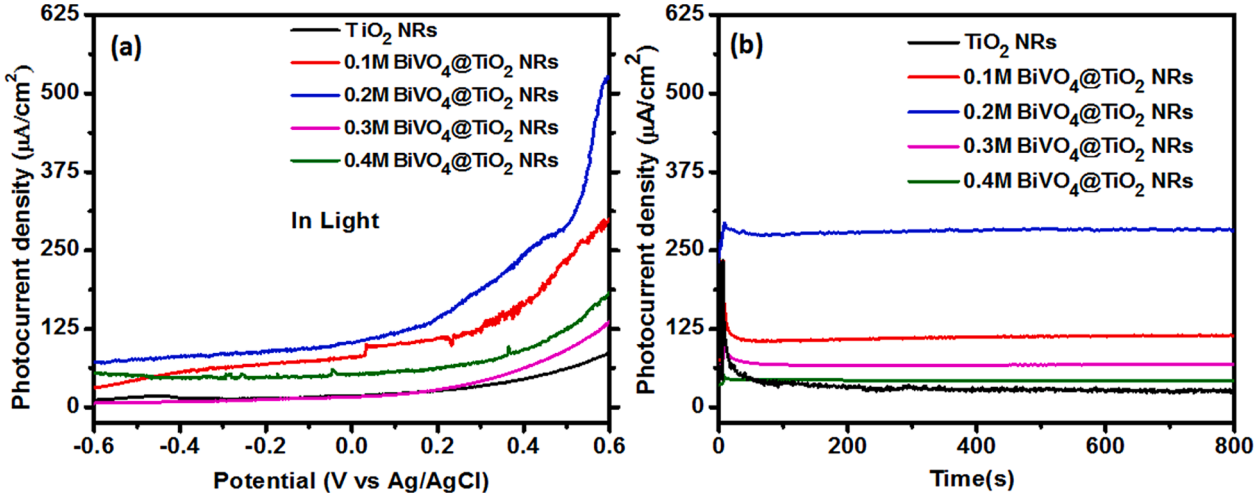

Fig. 8. a) linear sweep voltammetry and (b) chronoamperometry curves of 0.1 M, 0.2 M, 0.3 M and 0.4 M precursor concentrations for $BiVO_4$ deposition upon TiO_2 NRs at 150 °C.

because of well-developed $BiVO_4$ structure which is in good agreement with XRD and SEM results [46].

4.3. Photoelectrochemical Measurements.

To investigate the effect of deposition of $BiVO_4$ guest layer on un-doped and Fe doped rutile TiO_2 host layer, *J-V* curves were measured with stability profiles (*j-t*) to observe the transfer and injection of charges from $BiVO_4$ guest layer to un-doped and Fe doped TiO_2 host layer under illumination of 100 mW/cm^2 light intensity as shown in Fig. 8. Enhanced photocurrent density from 45μA/cm^2 for TiO_2 NRs to 363μA/cm^2 for 0.1 M $BiVO_4$@TiO_2 at 0.6 V vs. Ag/AgCl (1.23 vs RHE) was observed as depicted by Fig. 8a. Moreover, as the loading concentration of $BiVO_4$ is increased to 0.2 M, 0.3 M, and 0.4 M of the $BiVO_4$@TiO_2 heterojunction, the photocurrent density is found to be 520μA/cm^2, 94μA/cm^2, and 61μA/cm^2, respectively. Interestingly, 0.2 M $BiVO_4$@TiO_2 heterojunction shows the highest photocurrent density with optimized 0.2 M precursor concentration in comparison to loading concentrations of 0.3 M and 0.4 M for loading $BiVO_4$ over TiO_2 NRs due to core–shell TiO_2-$BiVO_4$ nanostructure formation with efficient interfacial charge transfer at the heterojunction. It elucidates that optimized loading of guest layer ($BiVO_4$ nanostructure) is necessary for fast electron/hole pair separation and their efficient transportation to host layers.

Noticeably, charge injection from guest layer to host layer also comprehend the interfacial importance of heterojunctions. Therefore, TiO_2 NRs were doped with 0.1%, 0.2% and 0.3% Fe and their individual photocurrent densities as well as in heterojunction were characterized. In Fig. S3, it is observed that 0.1%, 0.2% and 0.3% Fe-TiO_2 NRs showed photocurrent densities of 74μA/cm^2, 360μA/cm^2, and 137μA/cm^2 at 0.6 V vs. Ag/AgCl, respectively. It illustrates that 0.2% Fe doped TiO_2 NRs showed 8-folds photocurrent density in comparison to pristine TiO_2 NRs. Fe in TiO_2 NRs with 0.3% doping illustrated higher recombination of electron-hole pairs occur in comparison to 0.2% doping. These results demonstrated the successful insertion of extrinsic molecular orbitals/sub-states by doping of Fe into TiO_2 NRs [42,47].

Onset potential is an indicator to show better photocatalytic activity of the photoanodes. Normally, the lower the onset potential, better is the photocatalytic activity as it determines the charge injection at higher or lower overpotentials in the circuit. The onset potential of undoped TiO_2 NRs is found to be −0.12 V, while that of 0.1%, 0.2% and 0.3% Fe-TiO_2 NRs is found to be −0.60 V, −0.49 V, and −0.45 V, respectively as shown in Fig. S4. It is attributed to the reduction in band gaps by Fe doped TiO_2 NRs causing two factors; firstly, splitted molecular orbitals are introduced into conduction band and secondly, narrowing of band gap may also cause increase recombination rate of electron-hole pairs. Fe-doped TiO_2 has more chances to recombine its produced charges because of decrease in recombination resistance by addition of further splitted molecular orbitals. 0.3% doped TiO_2 has photocurrent density of 137μA/cm^2 with comparative high onset potential of −0.45 V than −0.49 V for 0.2% Fe doped TiO_2 as depicted in Fig. S4. Similarly, 0.1% Fe doped TiO_2 showed least onset potential of −0.60 V but its photocurrent output density is lower in comparison to 0.2% Fe-TiO_2 NRs. Highest photocurrent density of 360 μA/cm^2 in 0.2% Fe doped TiO_2 can be attributed to its smaller band gap leading to efficient electron/hole pair separation and charge transportation [48] in comparison to other Fe doped TiO_2 and undoped TiO_2 NRs.

Photostability of the anodes is a parameter to determine the photocorrosion of the anodes and its long-term stability for the photoelectrochemical hydrogen production. Fig. 8b shows that 0.2 M $BiVO_4$@TiO_2 NRs demonstrated highest photostability as well as photocurrent density in the whole-time duration of 800 s at 0.6 V vs Ag/AgCl reference electrode (1.23 vs. RHE) under one sun illumination, while other loadings of 0.1 M $BiVO_4$@TiO_2, 0.3 M $BiVO_4$@TiO_2, and 0.4 M $BiVO_4$@TiO_2 demonstrated excellent photostability but with lower photocurrent densities. These results are in good agreement with their photocurrents densities as shown in Fig. 8a. It is attributed to the core–shell structure with efficient charge transfer at the interface due to least recombination in individual lattice structures of 0.2 M $BiVO_4$@-TiO_2 NRs heterojunction and excellent homogeneity of $BiVO_4$ over TiO_2 NRs.

Therefore, optimized 0.2% Fe-TiO_2 was selected to proceed for further study to check the effect of synthesis temperature of the $BiVO_4$ over 0.2% Fe-TiO_2. For the purpose, J-V curves were obtained under standard one sun illumination for 0.2 M $BiVO_4$ synthesized at 150 °C, 175 °C and 200 °C upon optimized 0.2% Fe-TiO_2 NRs. Consequently, photocurrent densities of 0.78 mA/cm^2, 1.52 mA/cm^2, and 1.14 mA/cm^2 are observed for 0.2 M $BiVO_4$@0.2% Fe-TiO_2 synthesized at 150 °C, 175 °C and 200 °C while their onset potentials are observed to be −0.42 V, −0.59 V and −0.49 V, respectively as shown in Fig. 9a. While 0.2 M $BiVO_4$@ undoped TiO_2 synthesized at 150 °C showed its photocurrent density of 0.52 mA/cm^2 (Fig. 8a). It is observed that 0.2 M $BiVO_4$ photocatalyst synthesized at 175 °C upon 0.2% Fe-TiO_2 NRs shows highest photocurrent density with least onset potential. This is because of the crystallinity of the $BiVO_4$ synthesized at 175 °C with its homogeneous deposition upon 0.2% Fe-TiO_2 NRs and higher extraction capacity of photoexcited electrons of $BiVO_4$ by the 0.2% Fe-TiO_2 NRs in comparison to undoped TiO_2 NRs. On the other hand, $BiVO_4$ @0.2% Fe-TiO_2 NRs synthesized at 200 °C could not maintain its core–shell structure due to the development of $BiVO_4$ nanofibers over $BiVO_4$

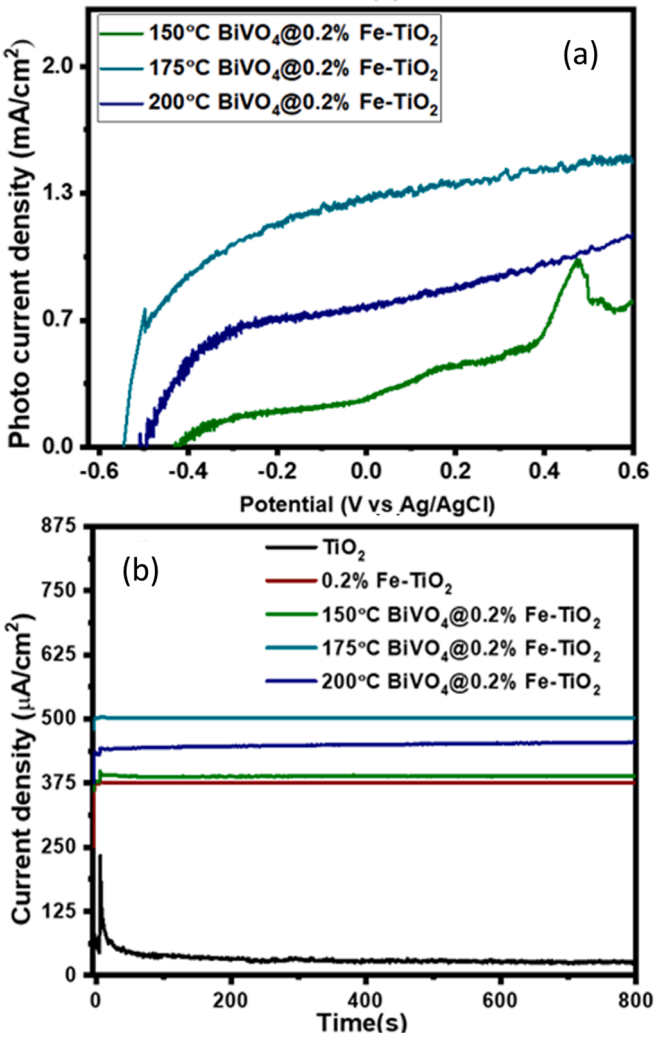

Fig. 9. (a) LSV curves and (b) chronoamperometry (J-t curves) of 0.2 M $BiVO_4$ deposition upon 0.2% Fe-TiO_2 NRs at 150 °C, 175 °C and 200 °C.

@0.2% Fe-TiO_2 NRs heterojunction, indicating higher recombination in $BiVO_4$ as observed in SEM images of Fig. 3. These results further illustrate that Fe doping in TiO_2 NRs introduced; extrinsic defects, oxygen vacancies and molecular orbitals below the conduction band minima that may provide a broader window for the flow of electrons from $BiVO_4$ to FTO via 0.2% Fe-TiO_2 NRs as compared to undoped TiO_2 NRs, which is in good agreement with the Mott-Schottky results. In other words, TiO_2 NRs are used only as charge transfer medium for the flow of hot photoexcited electrons from $BiVO_4$ to FTO, contrarily, 0.2% Fe-TiO_2 NRs not only utilized as charge transfer medium for the photoexcited electrons but also act as photocatalyst under visible region as it generates electron/hole pair by absorbing visible light along with $BiVO_4$ (as found in Fig. 5) and hence enhanced the overall photon capturing efficiency with excellent electron/hole pair separation and its efficient transportation to FTO via potential core–shell structured interfaces. The data presented in this study can be compared with the literature as given in the Table 1.

Moreover, in J-t curves as in Fig. 9b, the photocurrent densities are found to be 45 μA, 374μA, 389μA, 444.5μA and 510μA for TiO_2, 0.2% Fe-TiO_2, $BiVO_4$@Fe-TiO_2 NRs at 150C, $BiVO_4$@Fe-TiO_2 NRs at 200 C and $BiVO_4$@Fe-TiO_2 NRs at 175 C, respectively, at 0.6 V vs. Ag/AgCl reference electrode (1.23 V vs. RHE) under light intensity of 100 mW/cm^2 which are in good agreement with their linear sweep voltammetry results. It is noted that all the photo-anodes showed the good stability under light illumination for upto 800 s, showing simultaneous photon captures, electron/hole pair separation and transportation across the efficient interfaces of $BiVO_4$@Fe-TiO_2 NRs heterojunctions in comparison to $BiVO_4$@TiO_2 NRs heterojunctions (Fig. 8a and b). For pristine TiO_2, in first few minutes, the photocurrent increases and then rapidly decreases while this fall in photocurrent is very small in Fe modified TiO_2 samples and is almost negligible in 175 °C $BiVO_4$@Fe-TiO_2 photo-anode as it shows the stable j-t curve for 800 s (see Fig. 9b).

The impedance response and process of charge transfer between electrolyte and photo-anode were measured by using EIS in both dark and light under one sun intensity. It was investigated using frequency range of 100 kHz to 0.01 Hz under open circuit conditions in presence of 0.5 M Na_2SO_4 solution as an electrolyte under illumination of filtered visible light (100 mW/cm^2). Normally in Nyquist plots, smaller the diameter of semicircle shows lower charge transfer resistance across the electrode–electrolyte interface and vice versa. In Fig. S5a, the order of diameter of semicircle for concentrations of $BiVO_4$@TiO_2 photo-anode heterojunction is found to be 0.2 M < 0.4 M < 0.3 M < 0.1 M, indicating 0.2 M precursor concentrations for $BiVO_4$ deposition over TiO_2 NRs photo-anode provides least charge transfer resistance (R_{ct}) with least recombination rates of electron/hole pairs, which is in good agreement with the LSV results. Also, the lifetime of electrons can be calculated from typical Bode plot from its frequency. The peak frequency in Bode profile is the frequency that provides life time of electron/hole pairs and it is calculated using expression of $\tau_n = 1/(2\pi f_{min})$ [49]. Here f_{min} is the frequency on *x*-axis and τ_n is the lifetime for an electron/hole pair. The observed pattern for lifetime is found to be 0.2 M > 0.4 M > 0.3 M > 0.1 M in $BiVO_4$@TiO_2 photo-anode heterojunction, indicating the maximum lifetime of the photoexcited charge carriers in 0.2 M $BiVO_4$@TiO_2 photo-anode heterojunction as observed in the Bode plot of Fig. S5b. Also, the charge transfer resistance of 0.2% Fe-TiO_2 NRs is found to be least with smallest semicircle in Nyquist plots under dark and light conditions in comparison to pristine TiO_2 NRs, 0.1% Fe-TiO_2 NRs and 0.3% Fe-TiO_2 NRs as shown in Fig. S5c and Fig. S5d. The least charge transfer resistance with least recombination rate is observed in 0.2% Fe-TiO_2 NRs, that is due to its higher photon capturing tendency under visible light, efficient electron/hole pair separation and their fast transportation across the circuit in comparison to pristine TiO_2 NRs, 0.1% Fe-TiO_2 NRs and 0.3% Fe-TiO_2 NRs. These results are also in line with the LSV results. Bode plots in Fig. S5e and Fig. S5f, also show the significant difference of peak shift from 80 to 200 Hz under dark conditions to 0.05–1 Hz under light illumination for pristine TiO_2 NRs, 0.1% Fe-TiO_2 NRs, 0.2% Fe-TiO_2 NRs and 0.3% Fe-TiO_2 NRs, suggesting higher lifetime of the photoexcited electron under light illumination of one sun. Moreover, 5 mM Fe precursor concentration for 0.2% Fe-TiO_2 NRs shows least peak frequency of 59 Hz with corresponding highest lifetime of 2.6 ms for its photoexcited electrons in comparison to pristine TiO_2 NRs, 0.1% Fe-TiO_2 NRs, and 0.3% Fe-TiO_2 NRs.

Further in Fig. 10a and 10b, Nyquist plot has smallest semicircle for 0.2 M $BiVO_4$@0.2% Fe-TiO_2 photo-anode (with less imaginary and real resistance) than other photo-anodes, this shows the fast electron/hole pair separation and transfer of holes towards electrolyte and electrons towards FTO via efficient $BiVO_4$@0.2% Fe-TiO_2 photo-anode heterojunction (See Table 2). As shown in Fig. 10c and 10d the minimum frequency is of 0.2 M (175 °C) $BiVO_4$@0.2% Fe-TiO_2 and maximum for pure TiO_2 which identifies the maximum lifetime (0.05 s in light and 0.04 s in dark) of electron in modified bilayer hetero-junction sample and recombination is maximum for TiO_2 NRs. In case of bilayer heterocomposite of photo-anodes the 175 °C $BiVO_4$ @0.2% Fe-TiO_2 has minimum resistance with smallest semicircle as in Fig. 10a, b for both light and dark, on the same time it also has minimum frequency hence maximum lifetime 0.05 s of electrons (Fig. 10c and d). Other heterocomposites have higher resistance and larger semicircle as compare to this, similarly they also have larger frequency values which indicates the shorter electron lifetime.

Mott-Schottky analysis was conducted to determine the type of material, donor density and Flat band potentials of the photocatalyst as shown in Fig. S6a [50] under dark conditions. Its is observed that pristine TiO_2, 0.2% Fe-TiO_2, $BiVO_4$@Fe-TiO_2 NRs showed positive slopes indicating their n-type nature. The donor density is calculated using the equation,

$$\frac{1}{C^2} = \frac{2}{N_D} e\varepsilon_o\varepsilon\left[(E - E_{fb}) - \frac{kT}{e}\right] \quad (2)$$

Here, C is the semiconductor's space charge capacitance, e is elementary charge, $\varepsilon_\circ$ is space permittivity, $\boldsymbol{\varepsilon}$ is relative permittivity of TiO_2 and $BiVO_4$, E is applied potential, E_{fb} is flat band potential [51], N_D is donor density or charge carrier density, k is Boltzmann constant and T is temperature. It is observed that donor densities of 4.90×10^{12}, 6.39×10^{14}, 9.30×10^{17}, and 11.5×10^{19} cm^{-3} are observed for pristine TiO_2 NRs, 0.2% Fe-TiO_2 NRs, $BiVO_4$@TiO_2 NRs at $BiVO_4$@TiO_2 NRs at 150 °C and $BiVO_4$@Fe-TiO_2 NRs at 175 °C, respectively as presented in Table S2. For all samples the donor density was calculated using above equation [32] and data is presented in Table S2. These results indicate that Fe doping of TiO_2 NRs boosts the donor density of the photocatalysts even under dark conditions and provides a better replacement than pristine TiO_2 NRs as a substrate. It also supports the successful creation of extrinsic defects and oxygen vacancies in 0.2% Fe-TiO_2 NRs leading to enhanced donor densities. Also, $BiVO_4$ synthesized at 175 °C results in efficient charge transfer in comparison to the one synthesized at 150 °C. The slopes for Fe-TiO_2 and 175 °C $BiVO_4$@Fe-TiO_2 were smaller as compared to pristine TiO_2 which presents its increasing donor

Table 1
Literature data for the comparison with the state-of-the-art literature.

Sr#	Photoanode	Photocurrent density (mA/cm^2)	Applied Bias V vs RHE	Ref.
1	$BiVO_4$ /$CoNiO_2$	1.16	1.23 V	[26]
2	Rh_2O_3/ $BiVO_4$	3.5	1.23 V	[29]
3	$BiVO_4$/TiO_2	3.15	1.23 V	[28]
4	NiFeOOH/Co-Pi/ $BiVO_4$	2.03	1.23 V	[27]
5	$AgVO_3$/Mo-$BiVO_4$	1.93	1.23 V	[32]
6	$BiVO_4$@0.2 %Fe-TiO_2	1.52	1.23 V	This study
	$BiVO_4$@TiO_2	0.52	1.23 V	

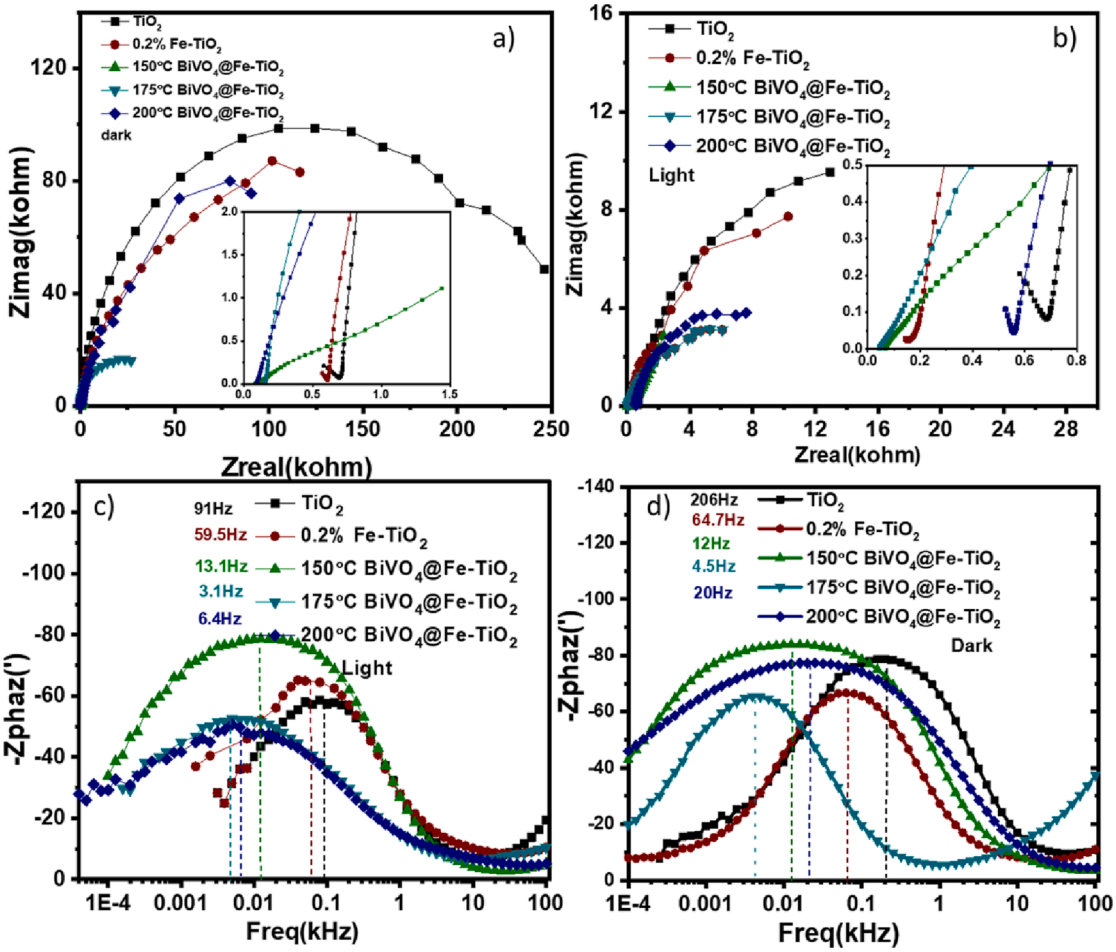

Fig. 10. Nyquist plots of $BiVO_4$@ Fe doped TiO_2 NRs at different temperatures a) in dark b) in light c) Bod plots of deposited $BiVO_4$ on Doped Nanorods of TiO_2 at three different temperatures to optimize the efficient photo anode in light d) bod in dark.

Table 2
EIS data from Nyquist plot under dark and light conditions using Randel's circuit.

Photocatalysts	R_s (kOhm) in dark	R_{ct} (kOhm) in dark	R_s (kOhm) in light	R_{ct} (kOhm) in light
Pristine TiO_2 NRs	0.63	287.58	0.7	32.62
0.2 %Fe-TiO_2 NRs	0.58	240.75	0.19	29.18
150 °C-0.2 M-$BiVO_4$ @TiO_2 NRs	0.18	141.74	0.074	21.44
175 °C-0.2 M-$BiVO_4$ @0.2 %Fe-TiO_2 NRs	0.17	76.37	0.059	11.78
200 °C-0.2 M-$BiVO_4$ @0.2 %Fe-TiO_2 NRs	0.12	186.29	0.58	16.49

density with lesser steep or less slope. The small donor density for Fe-TiO_2 as attributed to its additional orbitals and oxygen defects, in this way photo-generated electrons are unable to perform water splitting because its energy level is below the H_2O splitting reduction potential, hence its electron quenching is high. Although in case of $BiVO_4$@Fe-TiO_2 the donor density is high which indicates the larger lifetime of electrons in agreement with EIS (Bode) that is evidence of good electron transport [12,21]. Consequently, $BiVO_4$@Fe-TiO_2 NRs heterojunctions with doped TiO_2 NRs improved the overall charge carrier densities in comparison to $BiVO_4$@TiO_2 NRs heterojunctions without doping of TiO_2 NRs.

The flat-band potential level is determined for pristine TiO_2 NRs, 0.2% Fe-TiO_2 NRs, 0.2 M $BiVO_4$@TiO_2, and 175 °C $BiVO_4$@Fe-TiO_2 as −0.64 V, −0.68 V and −0.8 V, and −0.8 V respectively. A shift in Fermi level was indicated by negative shifting of flat band potential (E_{fb}) after doping with Fe. This shift in Fermi level may enhance the separation of charges at the interface of semiconductor and electrolyte [52]. The solar to hydrogen efficiency (STH) [53] was calculated using $\eta = \frac{I(1.23-V)}{Pin}$, where V is voltage vs RHE and P_{in} is 100mWcm^{-2}. The plot of STH % efficiency and voltage vs RHE is shown in Fig. S6b. Pristine TiO_2 and 0.2% Fe-TiO_2 both possess the optimum efficiency of 0.2% at 0.91 V and 0.48 V, respectively. Similarly, 0.2 M $BiVO_4$@TiO_2 exhibits the 0.6% at 0.45 V potential verses RHE and 0.2 M $BiVO_4$ @0.2% Fe-TiO_2 at 175 °C possess the STH efficiency of 1.12% at reduced voltage of 0.42 V vs RHE which directly indicates the higher capacity of solar light capturing, efficient electron/hole pair separations and fast transportation across the composite heterojunctions in 0.2 M $BiVO_4$ @0.2% Fe-TiO_2 at 175 °C in comparison to other studied photocatalysts which is in good agreement with XRD, SEM, LSV and EIS results.

A proposed mechanism from this study can be illustrated as shown in Fig. 11. After absorption of solar light, the electrons from VB of both TiO_2 and $BiVO_4$ may excite to respective CB after leaving holes in their valence bands (VB). As compare to $BiVO_4$@TiO_2 NRs, an efficient transport of charges occurs within Schottky barrier of heterojunction with type-II band alignment of TiO_2 [54,55]. The electrons move from CB of $BiVO_4$ to CB of TiO_2 and then towards counter electrode through substrate and reduce H^+ to H_2, while at the same time the holes from VB of TiO_2 transfers to VB of $BiVO_4$ due to the difference of work function of individual components of $BiVO_4$@TiO_2 NRs heterojunction. TiO_2 NRs only shows the intrinsic defects and did not have the capability to absorb visible regions but only UV region of the solar spectrum. TiO_2 acts as

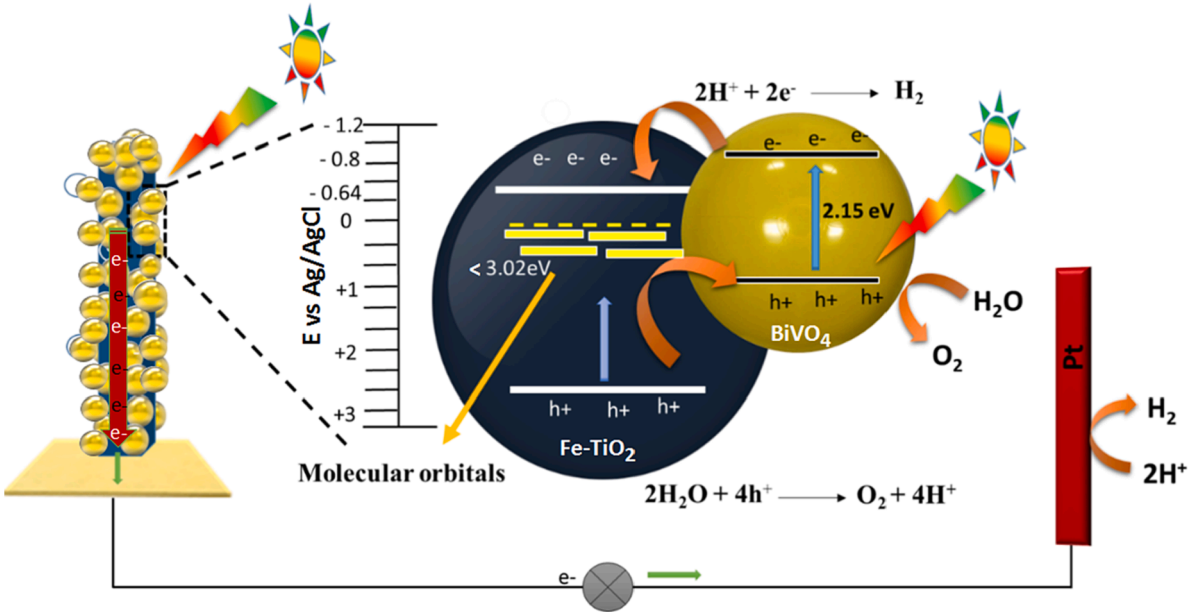

Fig. 11. Proposed mechanism of $BiVO_4$ @0.2% Fe-TiO_2 at 175 °C for photoexcited charge separation, extraction and transfer in photoelectrochemical cell.

substrate (to provide high surface area) and as well as provide a narrower charge transfer medium to the photoexcited electrons from $BiVO_4$ to FTO under illuminations due to its lower population of intrinsic defects. These factors may cause the poor collection of photoexcited charges of $BiVO_4$ to FTO via TiO_2 and subsequently lower charge transportation. Contrarily, after absorption of solar light the electrons from VB of both doped Fe-TiO_2 and $BiVO_4$ may excite to their respective CB after leaving holes in their VB. Noticeably, the doped Fe-TiO_2 NRs started absorbing visible light capturing due to extrinsic defects (introduced via Fe doping) works as a dual character. Firstly, it provides a broader capacity for the photoexcited electrons of $BiVO_4$ to reach FTO via Fe-TiO_2 NRs due to higher populations of defects. 2ndly, Fe-TiO_2 NRs itself absorb visible light and act as a co-catalyst instead of substrate. Thus, $BiVO_4$/Fe-TiO_2 NRs boosts its efficiency three folds of the type-II heterojunction in comparison to $BiVO_4$/TiO_2 NRs heterojunction. On the other hand, holes move in opposite direction to the electrons and oxidized the water at the photoanode with $BiVO_4$/Fe-TiO_2 NRs efficiently in comparison to $BiVO_4$/TiO_2 NRs. Hence, in type-II bilayer $BiVO_4$/Fe-TiO_2 NRs heterojunction, development of extrinsic defects due to Fe doping results in the stabilized interface, reduced photoexcited charge recombination, enhanced visible light harvesting, maximum charge carrier collection and fast transportation was observed. This strategy paved the way to develop more efficient interfaces with excellent photoelectrochemical water splitting efficiencies.

5. Conclusion

In this work, the $BiVO_4$@Fe-TiO_2 NRs with type-II heterojunction and extrinsic defects of TiO_2 NRs via Fe doping were developed for improved photoactivity. It results in faster electron/hole pair charge separation and transportation under illumination with 0.2% Fe doping in TiO_2 NRs which enhanced the photocurrent activity from 45μA for TiO_2 NRs to 360μA for 0.2% Fe-TiO_2 NRs. Also, 0.2 M $BiVO_4$@0.2 %Fe-TiO_2 showed highest photocurrent density of 1.52 mA/cm^2 in comparison to $BiVO_4$@undoped TiO_2 NRs with 0.52 mA/cm^2, and pristine TiO_2 NRs with 45μA/cm^2 at 0.6 V vs. Ag/AgCl (1.23 vs RHE) under 100 mW/cm^2 light intensity, which is 5 folds than the pristine TiO_2 NRs. Noticeably, 0.2% Fe doping in TiO_2 NRs provides broader electron collection and electron transfer flow to pass through it to counter electrode with least recombination rate upon loading of 0.2 M $BiVO_4$@0.2 % Fe-TiO_2 NRs in comparison to pristine TiO_2 NRs. It is concluded that 0.2% Fe doped TiO_2 NRs acts as efficient photoexcited electron collection and transfer medium as well as photocatalyst in comparison to undoped TiO_2 NRs. These results evidenced that optimized doping with extrinsic defects causes improved overall photocatalytic activity in type-II nanocomposites. Development of such efficient bilayer nanocomposite-based heterojunction paves the way to design tri/multilayer heterojunctions for improved efficiencies.

CRediT authorship contribution statement

Fazeelat Rehman: Validation, Investigation, Formal analysis, Data curation, Methodology, Writing – original draft, Writing – review & editing. **Noor Alam:** Validation, Methodology, Investigation, Formal analysis, Data curation. **Manzar Sohail:** Writing – review & editing, Validation, Methodology, Investigation. **Muhammad Ahmad:** Writing – review & editing, Visualization, Validation, Resources, Conceptualization. **Muhammad Israr Siddiqui:** Writing – review & editing, Visualization, Validation, Resources, Conceptualization. **Muhammad Imran Irshad:** Writing – review & editing, Visualization, Validation, Resources, Conceptualization. **Asad Mumtaz:** Writing – review & editing, Validation, Supervision, Software, Resources, Project administration, Methodology, Investigation, Funding acquisition, Conceptualization.

Declaration of Competing Interest

The authors declare that they have no known competing financial interests or personal relationships that could have appeared to influence the work reported in this paper.

Data availability

Data will be made available on request.

Acknowledgements

We acknowledge School of Natural Sciences (SNS), National University of Sciences and Technology (NUST), Islamabad for providing internal university funding. We also acknowledge funding of NRPU-HEC, Islamabad, Pakistan with the grant project #20-15769/NRPU/R&D/HEC/2021.

Appendix A. Supplementary data

Supplementary data to this article can be found online at https://doi.org/10.1016/j.jphotochem.2023.114956.

References

[1] I. Staffell, D. Scamman, A. Velazquez Abad, P. Balcombe, P.E. Dodds, P. Ekins, N. Shah, K.R. Ward, The role of hydrogen and fuel cells in the global energy system, Energ. Environ. Sci. 12 (2) (2019) 463–491.

[2] X. Zhang, H. Cui, M. Humayun, Y. Qu, N. Fan, X. Sun, L. Jing, Exceptional performance of photoelectrochemical water oxidation of single-crystal rutile TiO 2 nanorods dependent on the hole trapping of modified chloride, Sci. Rep. 6 (2016) 1–8.

[3] L. Yu, Z. Li, Y. Liu, F. Cheng, S. Sun, Enhanced photoelectrochemical performance of CdSe/Mn-CdS/TiO2 nanorod arrays solar cell, Appl. Surf. Sci. 309 (2014) 255–262.

[4] X. Chen, M. Wang, J. Chen, S. Shen, Electrophoretic deposition of nanostructured hematite photoanodes for solar hydrogen generation, J. Mater. Res. 31 (11) (2016) 1547–1553.

[5] J. Chen, W. Song, H. Hou, Y. Zhang, M. Jing, X. Jia, X. Ji, Ti3+ self-doped dark rutile TiO2 ultrafine nanorods with durable high-rate capability for lithium-ion batteries, Adv. Funct. Mater. 25 (43) (2015) 6793–6801.

[6] L. Shi, C. Xu, X. Sun, H. Zhang, Z. Liu, X. Qu, F. Du, Facile fabrication of hierarchical BiVO 4/TiO 2 heterostructures for enhanced photocatalytic activities under visible-light irradiation, J. Mater. Sci. 53 (16) (2018) 11329–11342.

[7] H.U. Lee, S.C. Lee, Y.-C. Lee, B. Son, S.Y. Park, J.W. Lee, Y.-K. Oh, Y. Kim, S. Choi, Y.-S. Lee, Innovative three-dimensional (3D) eco-TiO 2 photocatalysts for practical environmental and bio-medical applications, Sci. Rep. 4 (2014) 1–8.

[8] G. Lusvardi, C. Barani, F. Giubertoni, G. Paganelli, Synthesis and characterization of TiO2 nanoparticles for the reduction of water pollutants, Materials 10 (2017) 1208.

[9] J. Harris, R. Silk, M. Smith, Y. Dong, W.-T. Chen, G.I.N. Waterhouse, Hierarchical TiO2 nanoflower photocatalysts with remarkable activity for aqueous methylene blue photo-oxidation, ACS Omega 5 (30) (2020) 18919–18934.

[10] W. Qi, J. Du, Y. Peng, W. Wu, Z. Zhang, X. Li, K. Li, K. Zhang, C. Gong, M. Luo, H. Peng, Hydrothermal synthesis of TiO2 nanorods arrays on ITO, Mater. Chem. Phys. 207 (2018) 435–441.

[11] B. Cai, D. Zhong, Z. Yang, B. Huang, S. Miao, W.-H. Zhang, J. Qiu, C. Li, An acid-free medium growth of rutile TiO 2 nanorods arrays and their application in perovskite solar cells, J. Mater. Chem. C 3 (4) (2015) 729–733.

[12] V. Mahajan, S. Mohapatra, M. Misra, Stability of TiO2 nanotube arrays in photoelectrochemical studies, Int. J. Hydrogen Energy 33 (20) (2008) 5369–5374.

[13] J. Wan, R. Liu, Y. Tong, S. Chen, Y. Hu, B. Wang, Y. Xu, H. Wang, Hydrothermal etching treatment to rutile TiO 2 nanorod arrays for improving the efficiency of CdS-sensitized TiO 2 solar cells, Nanoscale Res. Lett. 11 (2016) 1–9.

[14] C. Schneider, N. Liu, P. Schmuki, Optimized FTO seeding enables the growth of highlyefficient Ta-doped TiO 2 nanorod photoanodes, Chem. Commun. 53 (72) (2017) 10050–10053.

[15] C. Yang, J. Qin, S. Rajendran, X. Zhang, R. Liu, WS2 and C-TiO2 nanorods acting as effective charge separators on g-C3N4 to boost visible-light activated hydrogen production from seawater, ChemSusChem 11 (23) (2018) 4077–4085.

[16] P. Subramanyam, B. Meena, V. Biju, H. Misawa, S. Challapalli, Emerging materials for plasmon-assisted photoelectrochemical water splitting, J Photochem Photobiol C: Photochem Rev 51 (2022) 100472.

[17] J. Tang, P. Wu, H. Sun, H. Jiang, Mo-doped BiVO4 modified with NH2-MIL-88B (Fe) cocatalyst overlayer for enhanced photoelectrochemical water oxidation, J. Photochem. Photobiol. A Chem. 431 (2022), 114049.

[18] N.Y. Tashkandi, S.M. Albukhari, A.A. Ismail, Visible-light driven of heterostructured LaFeO3/TiO2 photocatalysts for degradation of antibiotics: Ciprofloxacin as case study, J. Photochem. Photobiol. A Chem. 432 (2022) 114078.

[19] S. Patel, N. Gajbhiye, Room temperature magnetic properties of Cu-doped titanate, TiO2 (B) and anatase nanorods synthesized by hydrothermal method, Mater. Chem. Phys. 132 (2012) 175–179.

[20] D.-D. Qin, Y.-P. Bi, X.-J. Feng, W. Wang, G.D. Barber, T. Wang, Y.-M. Song, X.-Q. Lu, T.E. Mallouk, Hydrothermal growth and photoelectrochemistry of highly oriented, crystalline anatase TiO2 nanorods on transparent conducting electrodes, Chem. Mater. 27 (2015) 4180–4183.

[21] A. Mumtaz, N.M. Mohamed, M. Mazhar, M.A. Ehsan, M.S. Mohamed Saheed, Core–shell vanadium modified titania@ β-In2S3 hybrid nanorod arrays for superior interface stability and photochemical activity, ACS Appl. Mater. Interfaces 8 (14) (2016) 9037–9049.

[22] D. Shinde, S. Jagadale, R. Mane, R. Mane, V. Ghanwat, Time dependent facile hydrothermal synthesis of TiO 2 nanorods and their photoelectrochemical applications, J. Nanomed. Nanotechnol. S 7 (2015) 004.

[23] H. Chai, L. Gao, P. Wang, F. Li, G. Hu, J. Jin, In2S3/F-Fe2O3 type-II heterojunction bonded by interfacial SO for enhanced charge separation and transport in photoelectrochemical water oxidation, Appl. Catal. B 305 (2022) 121011.

[24] H. Chai, S. Wang, X.u. Wang, J. Ma, J. Jin, Modulation of the chemical microenvironment at the hematite-based photoanode interface with a covalent triazine framework for efficient photoelectrochemical water oxidation, ACS Catal. 12 (6) (2022) 3700–3709.

[25] K. Tian, L. Wu, H. Chai, L. Gao, M. Wang, H. Niu, L.i. Chen, J. Jin, Enhancement of charge separation and hole utilization in a Ni2P2O7-Nd-BiVO4 photoanode for efficient photoelectrochemical water oxidation, J. Colloid Interface Sci. 644 (2023) 124–133.

[26] G. Fang, Z. Liu, C. Han, X. Ma, H. Lv, C. Huang, Z. Cheng, Z. Tong, P. Wang, CoNiO 2 as a novel water oxidation cocatalyst to enhance PEC water splitting performance of BiVO 4, Chem. Commun. 56 (2020) 9158–9161.

[27] G. Fang, Z. Liu, C. Han, Enhancing the PEC water splitting performance of BiVO4 co-modifying with NiFeOOH and Co-Pi double layer cocatalysts, Appl. Surf. Sci. 515 (2020), 146095.

[28] B. Dong, F. Li, S. Feng, A visible-IR responsive BiVO 4/TiO 2 photoanode with multi-effect point defects for photothermal enhancement of photoelectrochemical water splitting, Chem. Commun. 58 (2022) 1621–1624.

[29] L.T. Gan, Y. Zhang, P.F. Liu, H.G. Yang, Enhanced surface kinetics and charge transfer of BiVO4 photoanodes by Rh2O3 cocatalyst loading for improved solar water oxidation, Chem. Asian J. 17 (2022) e202101359.

[30] S. Zhang, Z. Liu, D. Chen, Z. Guo, M. Ruan, Oxygen vacancies engineering in TiO2 homojunction/ZnFe-LDH for enhanced photoelectrochemical water oxidation, Chem. Eng. J. 395 (2020), 125101.

[31] T. Li, Y. Zou, Z. Liu, Magnetic-thermal external field activate the pyro-magnetic effect of pyroelectric crystal (NaNbO3) to build a promising multi-field coupling-assisted photoelectrochemical water splitting system, Appl Catal B 328 (2023), 122486.

[32] L. Gao, X. Long, S. Wei, C. Wang, T. Wang, F. Li, Y. Hu, J. Ma, J. Jin, Facile growth of AgVO3 nanoparticles on Mo-doped BiVO4 film for enhanced photoelectrochemical water oxidation, Chem. Eng. J. 378 (2019), 122193.

[33] S. He, Y. Meng, Y. Cao, S. Huang, J. Yang, S. Tong, M. Wu, Hierarchical Ta-Doped TiO2 Nanorod Arrays with Improved Charge Separation for Photoelectrochemical Water Oxidation under FTO Side Illumination, Nanomaterials 8 (2018) 983.

[34] A. Boucheham, A. Karaali, B. Rahal, Y. Belkacem, Characterization of Thermally Oxidized Ti6Al4V Alloys for Dental Application, (2017).

[35] B. Cao, J. Peng, Y. Xu, Simulated sunlight-driven degradation of rhodamine B by porous peanut-like TiO 2/BiVO 4 composite, J. Clust. Sci. 24 (2013) 771–785.

[36] S.H. Mohamed, M. El-Hagary, S. Althoyaib, Growth of undoped and Fe doped TiO 2 nanostructures and their optical and photocatalytic properties, Appl. Phys. A 111 (4) (2013) 1207–1212.

[37] N. Nasralla, M. Yeganeh, Y. Astuti, S. Piticharoenphun, N. Shahtahmasebi, A. Kompany, M. Karimipour, B. Mendis, N. Poolton, L. Šiller, Structural and spectroscopic study of Fe-doped TiO2 nanoparticles prepared by sol–gel method, Sci. Iran. 20 (2013) 1018–1022.

[38] H. Moradi, A. Eshaghi, S.R. Hosseini, K. Ghani, Fabrication of Fe-doped TiO2 nanoparticles and investigation of photocatalytic decolorization of reactive red 198 under visible light irradiation, Ultrason. Sonochem. 32 (2016) 314–319.

[39] M.A. Ismail, M.N. Hedhili, D.H. Anjum, V. Singaravelu, S.H. Chung, Synthesis and characterization of iron-doped TiO2 nanoparticles using ferrocene from flame spray pyrolysis, Catalysts 11 (2021) 438.

[40] M. Zalfani, B. van der Schueren, Z.-Y. Hu, J.C. Rooke, R. Bourguiga, M. Wu, Y.u. Li, G. Van Tendeloo, B.-L. Su, Novel 3DOM BiVO 4/TiO 2 nanocomposites for highly enhanced photocatalytic activity, J. Mater. Chem. A 3 (42) (2015) 21244–21256.

[41] P. Makuła, M. Pacia, W. Macyk, How to correctly determine the band gap energy of modified semiconductor photocatalysts based on UV–Vis spectra, in, ACS Publications 9 (23) (2018) 6814–6817.

[42] A.M. Huerta-Flores, G. Chávez-Angulo, O.A. Carrasco-Jaim, L.M. Torres-Martínez, M. Garza-Navarro, Enhanced photoelectrochemical water splitting on heterostructured α-Fe2O3-TiO2: X (X= Co, Cu, Bi) photoanodes: Role of metal doping on charge carrier dynamics improvement, J. Photochem. Photobiol. A Chem. 410 (2021), 113077.

[43] S. Challagulla, K. Tarafder, R. Ganesan, S. Roy, Structure sensitive photocatalytic reduction of nitroarenes over TiO 2, Sci. Rep. 7 (2017) 1–11.

[44] X. Qi, X. Zhu, J. Wu, Q. Wu, X. Li, M. Gu, Controlled synthesis of BiVO4 with multiple morphologies via an ethylenediamine-assisted hydrothermal method, Mater. Res. Bull. 59 (2014) 435–441.

[45] H. He, D. Sun, Q.i. Zhang, F. Fu, Y. Tang, J. Guo, M. Shao, H. Wang, Iron-doped cauliflower-like rutile TiO2 with superior sodium storage properties, ACS Appl. Mater. Interfaces 9 (7) (2017) 6093–6103.

[46] Y.M. Hunge, A. Uchida, Y. Tominaga, Y. Fujii, A.A. Yadav, S.-W. Kang, N. Suzuki, I. Shitanda, T. Kondo, M. Itagaki, M. Yuasa, S. Gosavi, A. Fujishima, C. Terashima, Visible Light-Assisted Photocatalysis Using Spherical-Shaped BiVO4 Photocatalyst, Catalysts 11 (4) (2021) 460.

[47] N. Denisov, J. Yoo, P. Schmuki, Effect of different hole scavengers on the photoelectrochemical properties and photocatalytic hydrogen evolution performance of pristine and Pt-decorated TiO2 nanotubes, Electrochim. Acta 319 (2019) 61–71.

[48] J. Liu, H. Yang, W. Tan, X. Zhou, Y. Lin, Photovoltaic performance improvement of dye-sensitized solar cells based on tantalum-doped TiO2 thin films, Electrochim. Acta 56 (1) (2010) 396–400.

[49] D. Loveday, P. Peterson, B. Rodgers, Evaluation of organic coatings with electrochemical impedance spectroscopy, JCT Coatings Tech 8 (2004) 46–52.

[50] T.R.C.K. Wijayarathna, G.M.L.P. Aponsu, Y.P.Y.P. Ariyasinghe, E.V.A. Premalal, G. K.R. Kumara, K. Tennakone, A high efficiency indoline-sensitized solar cell based on a nanocrystalline TiO2 surface doped with copper, Nanotechnology 19 (48) (2008) 485703.

[51] S. Sakthivel, H. Kisch, Daylight photocatalysis by carbon-modified titanium dioxide, Angew. Chem. Int. Ed. 42 (40) (2003) 4908–4911.

[52] W. Zhou, T. Jiang, Y. Zhao, C. Xu, C. Pei, H.J.J.o.c. Xue, i. science, Ultrathin TiO2/BiVO4 nanosheet heterojunction arrays modified with NiFe-LDH nanoparticles for enhanced photoelectrochemical oxidation of water, 549 (2019) 42-49.

[53] O. Monfort, D. Raptis, L. Satrapinskyy, T. Roch, G. Plesch, P. Lianos, Production of hydrogen by water splitting in a photoelectrochemical cell using a BiVO4/TiO2 layered photoanode, Electrochim. Acta 251 (2017) 244–249.
[54] S.S. Kalanur, I.-H. Yoo, J. Park, H.J.J.o.M.C.A. Seo, Insights into the electronic bands of WO 3/BiVO 4/TiO 2, revealing high solar water splitting efficiency, 5 (2017) 1455-1461.
[55] B.-Y. Cheng, J.-S. Yang, H.-W. Cho, J.-J.J.A.a.m. Wu, interfaces, Fabrication of an efficient BiVO4–TiO2 heterojunction photoanode for photoelectrochemical water oxidation, 8 (2016) 20032-20039.